

Turbulent channel flow near maximum drag reduction: simulations, experiments and mechanisms

By P. K. PTASINSKI¹†, B. J. BOERSMA¹,
F. T. M. NIEUWSTADT¹‡, M. A. HULSEN²,
B. H. A. A. VAN DEN BRULE³ AND J. C. R. HUNT^{1,4}

¹J.M. Burgers Centre for Fluid Dynamics, Delft University of Technology,
Leeghwaterstraat 21, 2628 CA Delft, The Netherlands

²Materials Technology, Eindhoven University of Technology,
PO Box 513, 5600 MB Eindhoven, The Netherlands

³Shell International Exploration and Production BV,
Volmerlaan 6, 2288 GD Rijswijk, The Netherlands

⁴Department of Space and Climate Physics, University College London,
Gower Street, London WC1E 6BT, UK

(Received 22 November 2002 and in revised form 23 April 2003)

It is well known that the drag in a turbulent flow of a polymer solution is significantly reduced compared to Newtonian flow. Here we consider this phenomenon by means of a direct numerical simulation of a turbulent channel flow. The polymers are modelled as elastic dumbbells using the FENE-P model. In the computations the polymer model is solved simultaneously with the flow equations, i.e. the polymers are deformed by the flow and in their turn influence the flow structures by exerting a polymer stress. We have studied the results of varying the polymer parameters, such as the maximum extension, the elasticity and the concentration. For the case of highly extensible polymers the results of our simulations are very close to the maximum drag reduction or Virk (1975) asymptote. Our simulation results show that at approximately maximum drag reduction the slope of the mean velocity profile is increased compared to the standard logarithmic profile in turbulent wall flows. For the r.m.s. of the streamwise velocity fluctuations we find initially an increase in magnitude which near maximum drag reduction changes to a decrease. For the velocity fluctuations in the spanwise and wall-normal directions we find a continuous decrease as a function of drag reduction. The Reynolds shear stress is strongly reduced, especially near the wall, and this is compensated by a polymer stress, which at maximum drag reduction amounts to about 40% of the total stress. These results have been compared with LDV experiments of Ptasinski *et al.* (2001) and the agreement, both qualitatively and quantitatively, is in most cases very good. In addition we have performed an analysis of the turbulent kinetic energy budgets. The main result is a reduction of energy transfer from the streamwise direction, where the production of turbulent kinetic energy takes place, to the other directions. A substantial part of the energy production by the mean flow is transferred directly into elastic energy of the polymers. The turbulent velocity fluctuations also contribute energy to the polymers. The elastic energy of the polymers is subsequently dissipated by polymer relaxation.

† Present address: Akzo Nobel Chemicals bv, dept. CPT, P.O. Box 9300, 6800 SB Arnhem, the Netherlands.

‡ Author to whom correspondence should be addressed: f.nieuwstadt@wbmt.tudelft.nl.

We have also computed the various contributions to the pressure fluctuations and identified how these change as a function of drag reduction. Finally, we discuss some cross-correlations and various length scales. These simulation results are explained here by two mechanisms. First, as suggested by Lumley (1969) the polymers damp the cross-stream or wall-normal velocity fluctuations and suppress the bursting in the buffer layer. Secondly, the ‘shear sheltering’ mechanism acts to amplify the streamwise fluctuations in the thickened buffer layer, while reducing and decoupling the motions within and above this layer. The expression for the substantial reduction in the wall drag derived by considering the long time scales of the nonlinear fluctuations of this damped shear layer, is shown to be consistent with the experimental data of Virk *et al.* (1967) and Virk (1975).

1. Introduction

The character of turbulence in a dilute polymer solution differs substantially from that in Newtonian fluids. Since the discovery by Toms (1949) that addition of a small amount of long-chain polymers to a turbulent pipe or channel flow results in a significant reduction of frictional drag, this phenomenon has attracted much attention both from the applied and fundamental point of view. Since turbulence consists of a large range of spatial scales, one might expect that because of their small size polymers could only influence the smallest or micro-scales of turbulence by changing the effective viscosity and that flow processes which primarily depend on the large macro-scales would remain unaffected. However, the effect of drag reduction implies that the polymers are able to fundamentally change the large-scale turbulent statistics and structures, especially in the buffer layer. Despite this phenomenon being well known for more than 50 years and widely applied in practice, a convincing physical explanation and quantitative models are both still lacking.

Over the past 50 years numerous papers have been written, discussing experimental, numerical and theoretical aspects of the subject. For a general review the reader is referred to Lumley (1969) and to the more recent work of Gyr & Bewersdorff (1995). Two principal theoretical concepts have been put forward to explain the phenomenon of drag reduction by polymers. The first can be attributed to Lumley (1969, 1973), who proposed a mechanism based on the extension of the polymers. He postulated that stretching of randomly coiled polymers, primarily in regions with strong deformations such as the buffer layer, increases the effective (extensional) viscosity. The result is damping of small eddies, a thickening of the viscous sublayer and consequently drag reduction. Lumley also mentions that the influence of the polymers on the turbulence only becomes important when the time scale of the polymers (e.g. the relaxation time) becomes larger than the time scale of the flow, which is known as the onset of drag reduction. The second theory, attributed to de Gennes (1990), is that drag reduction is caused by the elastic rather than the viscous properties of polymers. This idea is supported by experiments showing that drag reduction also occurs when the polymers have been injected in the centre of the pipe (e.g. McComb & Rabie 1979, 1982). However, these authors establish that in these cases drag reduction is a wall effect localized in the buffer layer. De Gennes’ explanation is that the shear waves which are caused by the elasticity of the polymers prevent production of turbulent velocity fluctuations at the small scales. Both theories, however, are somewhat qualitative and they fail to explain the dynamics of wall turbulence quantitatively.

A major result in polymer drag reduction was obtained by Virk *et al.* (1967), Virk, Mickley & Smith (1970) and Virk (1975). They observed that the amount of drag reduction is limited by an empirical asymptote, called the mean drag reduction asymptote (MDR) or Virk asymptote. This means that for each value of the Reynolds number the friction is limited by a lower bound. The asymptote was originally proposed for polymer solutions, for which the shear viscosity could be taken as constant and equal to that of the solvent, but by a small modification of the Reynolds number it can be generalized to more concentrated solutions for which the viscosity of the solution is no longer constant (Gyr & Bewersdorff 1995, p. 105).

From the various other experimental contributions that have been published we should mention here Laser Doppler Velocimetry (LDV) measurements in channel flow (Harder & Tiederman 1991; Wei & Willmarth 1992; Willmarth, Wei & Lee 1987) and pipe flow (Pinho & Whitelaw 1990; den Toonder, Nieuwstadt & Kuiken 1995; den Toonder *et al.* 1997). In all these experiments similar changes are observed for mean velocity, turbulence intensities and Reynolds stresses. However, these experiments have all been carried out in dilute polymer solutions for which the amount of drag reduction is not near the MDR. Experimental data at higher values of drag reduction are reported by Gampert & Yong (1989) for duct flow and by Warholic, Massah & Hanratty (1999a) and Warholic *et al.* (2001) for channel flow. The latter suggest that for maximum drag reduction the Reynolds stress almost vanishes and this has the implication that polymers produce rather than dissipate turbulent kinetic energy. Ptasinski *et al.* (2001) have carried out pipe flow experiments close to the MDR. Their main result is that the addition of polymers significantly modifies the turbulence statistics. They also find that the turbulent shear stress is substantially suppressed but that it remains definitely non-zero. The decrease of the turbulent stresses is primarily compensated by an increase of the polymer stresses. We will discuss these experiments in more detail in connection with the presentation of our simulation results. Other experiments indicate that polymer additives suppress the appearance of strong vortices and reduce the formation of large eddies (Bonn *et al.* 1993; Cadot, Douady & Couder 1995; Douady, Couder & Brachet 1991).

With increasing computer capabilities and the development of advanced viscoelastic models, it has become possible to perform direct numerical simulations (DNS) of turbulent drag reducing flows. The advantage of this approach is that one can more easily isolate and study the effect of various polymer properties (like elasticity, stretching and concentration) on the flow. Moreover, simulations provide quantities like pressure and two-point correlations which are difficult to obtain experimentally and which offer additional insight into the mechanism of polymeric drag reduction. Generally it is assumed that polymers in turbulent flow must be highly stretched before they can effectively change the turbulence (Hinch 1977). Based on this assumption, Orlandi (1995) performed a direct numerical simulation by coupling the extensional viscosity to the local deformation of the flow and by proposing an anisotropic stress model. A similar approach was used by den Toonder *et al.* (1995, 1997) who confirm that a high elongational viscosity is important. In these studies it is assumed that a highly stretched polymer orients itself into the flow direction while exerting a viscous anisotropic stress in this direction.

These simulations lead to drag reduction and have been able to confirm the experimental observations at least qualitatively. However, these models are still quite simple and for instance do not take relaxational effects of the polymers into account. Massah *et al.* (1993) and Massah & Hanratty (1997) studied the configurational changes of single polymer molecules in simple rheological shear and elongational

flows and in turbulent flows by representing the polymers as FENE bead–spring chains. These studies reconfirm the unraveling of the polymers by strong straining deformations. In addition they show that the polymer configuration changes mainly in the buffer layer and that polymers introduce additional stresses associated with their stretching. However, in these simulations only the influence of the turbulence on the polymers is considered and not the effect of the polymers back on the flow. Sureshkumar, Beris & Handler (1997) and Dimitropoulos, Sureshkumar & Beris (1998) have performed a DNS in combination with a more realistic polymer model, the so-called FENE-P model, which we will discuss in detail in the following. These simulations, which have been carried out for cases representative of dilute polymer concentrations, predict a drag reduction and a change in turbulence statistics comparable to what is found in the experiments. They also provide some criteria for the onset of drag reduction. The FENE-P model could also be applicable to fibres which cause drag reduction (McComb & Chan 1985), though the effect is different than for polymers since fibres are stiff and cannot be extended from a coiled configuration.

No numerical simulations have been performed for the high drag reduction regime, although the results of Warholic *et al.* (1999a, 2001) and Ptasinski *et al.* (2001) indicate that the polymer behaviour near the maximum drag reduction asymptote has major consequences for the turbulence. Therefore, in the current study we have performed direct numerical simulations of turbulent channel flow with polymers close to the maximum drag reduction or Virk asymptote. We are able to reach this regime by use of a rather high Reynolds number, together with high polymer concentrations and strongly extensible polymers. Our objective is to interpret the effects of polymers on turbulence in this regime and to suggest a mechanism for the drag reduction. We compare our findings with those obtained for Newtonian flow and with experimental data obtained at large drag reduction, in particular the data of Ptasinski *et al.* (2001). Furthermore, we focus on the polymer contribution to the total stress and discuss its influence on the kinetic energy of the mean flow and the turbulence. We also consider the budget of the elastic energy of the polymers. Finally, we discuss cross-correlations and various length scales in the flow and set up a hypothesis for a buffer layer mechanism to explain the behaviour of the friction coefficient near the maximum drag reduction asymptote.

The outline of this paper is as follows. In §2 we describe the governing equations for the flow and the constitutive equations for the FENE-P model. The numerical procedures of the simulations and the numerical parameters of the flow, the polymers and the geometry are given in §3. In §4 we present the results for the flow statistics, such as first- and second-order velocity statistics, extension of the polymers and various shear stress contributions together with a comparison with experiments of Ptasinski *et al.* (2001). In §5 we focus on the kinetic energy and its connection with the elastic energy of the polymers. In §6 we deal with the pressure and its influence on the flow. In §7 we discuss cross-correlations and various length scales and the behaviour of the friction coefficient in the high drag reduction regime. Finally the main conclusions are drawn in §8.

2. Governing equations

We consider the isothermal flow of an incompressible fluid in an orthogonal Cartesian coordinate system (x, y, z) for the streamwise (mean flow), spanwise and wall-normal directions respectively. The general equations are given by the continuity

equation and the equation for the conservation of momentum:

$$\nabla \cdot \mathbf{u} = 0, \quad (2.1)$$

$$\rho \frac{D\mathbf{u}}{Dt} \equiv \rho \frac{\partial \mathbf{u}}{\partial t} + \rho \mathbf{u} \cdot \nabla \mathbf{u} = -\nabla p + \nabla \cdot \boldsymbol{\tau}. \quad (2.2)$$

In these equations \mathbf{u} is the velocity vector, t is the time, ρ is the density and $\boldsymbol{\tau}$ is the total extra stress tensor. D/Dt denotes the material derivative. The fluid that we consider is a polymer solution, which is a mixture of a Newtonian solvent in which long-chain linear polymer molecules are dissolved. In order to obtain a full solution, a relation is needed between the stress and the deformation history. To this end we take the total stress to be the sum of a Newtonian part due to the solvent ($\boldsymbol{\tau}^{(s)}$) and a non-Newtonian part due to the polymers ($\boldsymbol{\tau}^{(p)}$) according to

$$\boldsymbol{\tau} = \boldsymbol{\tau}^{(s)} + \boldsymbol{\tau}^{(p)} = \beta \eta_0 (\nabla \mathbf{v} + (\nabla \mathbf{v})^T) + \boldsymbol{\tau}^{(p)}, \quad (2.3)$$

where $\beta = \eta_s/\eta_0$, the ratio of the solvent viscosity η_s to the total zero-shear-rate viscosity of the solution η_0 .

The polymer contribution to the stress ($\boldsymbol{\tau}^{(p)}$) must be related to the flow field and to the polymer configuration. For this a polymer model is needed which is able to describe the polymer dynamics in a turbulent flow realistically. Here, we consider the so-called elastic dumbbell model, which has its origin in kinetic theory (Bird *et al.* 1987). In this theory the polymers are considered as small mechanical objects (the dumbbells) and this allows us to calculate rheological properties such as the stress-strain relationship. The elastic dumbbell is represented by two spherical beads with mass m connected by a non-bendable spring. The configuration of a dumbbell is fully specified by its length and its direction, which is represented by the vector \mathbf{Q} . Although molecular architecture and internal configurations are neglected, the model contains two essential characteristics of linear polymers, namely orientability and stretchability. These properties are essential to describe the rheological properties of the polymer solution.

The polymer stress tensor consists of a contribution from the intramolecular potential (the connecting spring) and a contribution from the motion of the beads. From kinetic theory, the so-called Kramers expression for this stress can be derived (Bird *et al.* 1987, p. 69). It consists of an isotropic equilibrium value and a deviation from this equilibrium value due to flow. Only the latter is dynamically significant and is therefore the extra polymeric stress $\boldsymbol{\tau}^{(p)}$ introduced in (2.3). It is given by

$$\boldsymbol{\tau}^{(p)} = -nkT\mathbf{I} + n\langle \mathbf{Q}\mathbf{F}^{(c)} \rangle, \quad (2.4)$$

where n is the number of polymers per unit volume, k is the Boltzmann constant, T is the absolute temperature and $\mathbf{F}^{(c)}$ is the retractive force of the spring. The brackets $\langle \cdot \rangle$ denote an average over the distribution function which gives the probability of all dumbbell configurations. In a condition of no flow (2.4) reduces to zero.

The dumbbells are convected through the flow and are deformed by forces due to straining by the flow. Convection is related to the motion of the centre of mass of the dumbbells while the deformation changes the dumbbell configuration, i.e. the orientation and the separation of the beads. From these forces equations of motion for the beads can be derived and this leads to an evolution equation for the conformation tensor $\langle \mathbf{Q}\mathbf{Q} \rangle$. The forces experienced by the beads are the hydrodynamic Stokes drag force, the force due to Brownian motion (because of thermal fluctuations the beads experience rapid and irregular accelerations) and the spring or connector force, which is the result of the intramolecular potential of the dumbbell. Inertia is neglected

because of the small mass of the beads and their slow motion through the solvent. The evolution equation for the conformation tensor $\langle \mathbf{Q}\mathbf{Q} \rangle$ is

$$\begin{aligned} \frac{D\langle \mathbf{Q}\mathbf{Q} \rangle}{Dt} &\equiv \frac{\partial \langle \mathbf{Q}\mathbf{Q} \rangle}{\partial t} + \mathbf{u} \cdot \nabla \langle \mathbf{Q}\mathbf{Q} \rangle \\ &= \nabla \mathbf{u} \cdot \langle \mathbf{Q}\mathbf{Q} \rangle + \langle \mathbf{Q}\mathbf{Q} \rangle \cdot (\nabla \mathbf{u})^T + \frac{4kT}{\zeta} \mathbf{I} - \frac{4}{\zeta} \langle \mathbf{Q}\mathbf{F}^{(c)} \rangle. \end{aligned} \quad (2.5)$$

On second line of the right-hand side, the first two terms represent deformation by hydrodynamic forces, the third term refers to Brownian motion and the fourth term is the elastic retraction of the spring. The parameter ζ is the Stokes friction coefficient of the beads.

Up to now we have discussed the elastic dumbbell theory without specifying the connector force. One of the most common and realistic models is based on a finitely extensible nonlinear elastic (FENE) spring which was introduced by Warner (1972). In this paper, we use a modification of the FENE model proposed by Bird, Dotson & Johnson (1980), which is called the FENE-P model. For the FENE-P model the connector force $\mathbf{F}^{(c)}$ is

$$\mathbf{F}^{(c)} = \frac{H\mathbf{Q}}{1 - \langle Q^2 \rangle / Q_0^2}, \quad (2.6)$$

where H is the spring constant, Q_0 is the maximum separation of the beads and $\langle Q^2 \rangle = \text{tr} \langle \mathbf{Q}\mathbf{Q} \rangle$ is the ensemble squared averaged length of the polymer. This pre-averaging in the de-nominator of equation (2.6), which is known as the Peterlin approximation and which distinguishes the FENE-P from the FENE model, allows us to obtain a closed-form expression for (2.4) for the polymer stress $\boldsymbol{\tau}^{(p)}$ in terms of $\langle \mathbf{Q}\mathbf{Q} \rangle$ for which a separate closed-form equation (2.5) is available.

Let us scale the dumbbell vector with the length $\sqrt{kT/H}$, so that $\tilde{\mathbf{Q}} = \mathbf{Q} / \sqrt{kT/H}$. This allows us to introduce a dimensionless length parameter $b = H Q_0^2 / kT$. Furthermore we introduce the relaxation time of the dumbbell $\lambda = \zeta / 4H$ and the conformation tensor $\mathbf{c} = \langle \tilde{\mathbf{Q}}\tilde{\mathbf{Q}} \rangle$. Equations (2.4) and (2.5) combined with the dumbbell force (2.6) then lead to the following equations for the polymer stress:

$$\boldsymbol{\tau}^{(p)} = nkT (-\mathbf{I} + f\mathbf{c}) \quad (2.7)$$

and

$$\frac{\partial \mathbf{c}}{\partial t} = -\mathbf{u} \cdot \nabla \mathbf{c} + \nabla \mathbf{u} \cdot \mathbf{c} + \mathbf{c} \cdot (\nabla \mathbf{u})^T + \frac{1}{\lambda} (\mathbf{I} - f\mathbf{c}), \quad (2.8)$$

with

$$f = \left(1 - \frac{1}{b} \text{tr} \mathbf{c} \right)^{-1}. \quad (2.9)$$

We find that the polymer stress is characterized by three parameters: the relaxation time λ , the length parameter b and the parameter nkT which is related to the viscosity ratio β . The relation between β and the parameter nkT (determining the polymer concentration) is used in order to compute the polymer stress in (2.7) and according to Wedgewood & Bird (1988) is

$$\eta_p = (1 - \beta)\eta_0 = nkT\lambda \frac{b}{b + 3}. \quad (2.10)$$

where η_p is called the polymer viscosity. The conservation equations (2.1)–(2.3) together with (2.7)–(2.9) form a closed set of equations and their numerical solution will be discussed in the next section.

3. Numerical algorithm and parameters

3.1. Computational procedures

For the numerical solution we discretize equations (2.1), (2.2) and (2.8) on a three-dimensional grid and integrate them in time. The flow geometry is a channel with height H and the flow is considered to be fully turbulent. The wall shear stress is τ_w from which we obtain the friction velocity $u_* = \sqrt{\tau_w/\rho}$ with ρ the fluid density. Let us introduce dimensionless variables, $\tilde{x} = x/H$, $\tilde{\mathbf{u}} = \mathbf{u}/u_*$ and $\tilde{t} = tu_*/H$. The pressure and the polymer stress tensor are made dimensionless with ρu_*^2 . This gives the following equation for the conservation of momentum:

$$\frac{\partial \tilde{\mathbf{u}}}{\partial \tilde{t}} = -\tilde{\mathbf{u}} \cdot \tilde{\nabla} \tilde{\mathbf{u}} - \tilde{\nabla} \tilde{p} + \beta \frac{1}{Re_*} \tilde{\nabla}^2 \tilde{\mathbf{u}} + \tilde{\nabla} \cdot \tilde{\boldsymbol{\tau}}^{(p)}, \quad (3.1)$$

where $Re_* = \rho u_* H / \eta_0$ is the Reynolds number. The evolution equation for the conformation tensor becomes

$$\frac{\partial \mathbf{c}}{\partial \tilde{t}} = \underbrace{-\tilde{\mathbf{u}} \cdot \tilde{\nabla} \mathbf{c} + \tilde{\nabla} \tilde{\mathbf{u}} \cdot \mathbf{c} + \mathbf{c} \cdot (\tilde{\nabla} \tilde{\mathbf{u}})^T}_{G(\mathbf{u}, \mathbf{c})} + \underbrace{\frac{1}{\tilde{\lambda}} \mathbf{I} - \frac{1}{\tilde{\lambda}} \mathbf{f} \mathbf{c}}_{H(\mathbf{c})}, \quad (3.2)$$

where $\tilde{\lambda} = \lambda u_*/H$ is the dimensionless relaxation time. Note that the tensor $\mathbf{c} = \langle \tilde{\mathbf{Q}} \tilde{\mathbf{Q}} \rangle$ is already dimensionless. From now on we will drop the tilde symbol and consider these equations in their non-dimensional form only.

The system of equations is discretized using a pseudospectral method in the streamwise (x) and spanwise (y) directions and a finite difference method in the wall-normal (z) direction. Periodic boundary conditions are applied in the two homogeneous directions and no-slip boundary conditions on the two channel walls. We use a staggered grid, so that the pressure and the x - and y -velocity components are determined in the centres of the gridcells, while the z -velocity component is determined at the cell walls. For the conformation tensor \mathbf{c} and the polymer stress tensor $\boldsymbol{\tau}^{(p)}$ we define the xz - and yz -components at the cell walls and the other four components in the cell centres. In this way we obtain an accurate discretization of all gradients in the wall-normal direction.

The integration of the discretized equations does not necessarily produce a positive definite value for the tensor \mathbf{c} . However, positive definiteness of this tensor is essential (see Dupret & Marchal 1986) as it is related to the (positive) length of the polymers. The violation of this constraint may occur in the numerical solution of time-dependent viscoelastic flow problems and becomes worse as elasticity effects become more important. To avoid this problem a small artificial diffusive term is added to the equation for the conformation tensor in order to improve the stability of the computations (see Sureshkumar *et al.* 1997). More precisely, we add an extra term $\kappa/(u_*H) \nabla^2 \mathbf{c}$ to term $G(\mathbf{u}, \mathbf{c})$ of equation (3.2). The diffusivity κ should be small compared to the relaxational diffusivity H^2/λ , or $\kappa\lambda/H^2 \ll 1$. Furthermore the effect of this diffusive term should approach zero when the grid size and time step decrease. In our case we have taken $\kappa/(u_*H) = 1.2 \times 10^{-2}$. It should be stressed that the introduction of the artificial stress diffusivity is necessary for numerical stability reasons only. In the Appendix we study the effect of varying this diffusivity for selected results and show that a small variation does not significantly modify our results. A detailed analysis on the addition of the stress diffusivity has been performed by Sureshkumar & Beris (1995) and Sureshkumar *et al.* (1997), who used a value of $\kappa/(u_*H) = \mathcal{O}(10^{-2})$.

The momentum equations are integrated in time using a second-order Adams–Bashforth method for the advective, diffusive and polymer terms with the standard pressure correction method to enforce continuity. The time step is determined using the Courant criterion.

For the integration of the discretized equation for the polymer conformation tensor, which is solved simultaneously with the continuity and the momentum equations, we use a second-order Adams–Bashforth scheme for the advection and the deformation due to the flow and a second-order Adams–Moulton scheme for the FENE-P force in order to prevent the dumbbells from exceeding their maximum length, i.e. $\text{tr}\mathbf{c} < b$. This leads to the following discrete equation:

$$\mathbf{c}^{n+1} = \mathbf{c}^n + \Delta t \left(\frac{3}{2}G^n - \frac{1}{2}G^{n-1} + \frac{1}{2}H^n + \frac{1}{2}H^{n+1} \right), \quad (3.3)$$

where $G(\mathbf{u}, \mathbf{c})$ (including the artificial diffusion term) and $H(\mathbf{c})$ are given by equation (3.2). The resulting expression for \mathbf{c} at the new time step then becomes

$$\mathbf{c}^{n+1} \left(1 + \frac{\Delta t}{2\lambda} \frac{1}{1 - (\text{tr}\mathbf{c}^{n+1})/b} \right) = \mathbf{c}^n + \Delta t \left(\frac{3}{2}G^n - \frac{1}{2}G^{n-1} + \frac{1}{2}H^n \right). \quad (3.4)$$

Taking the trace of this equation and rearranging the terms leads to a quadratic equation for $\text{tr}\mathbf{c}^{n+1}$ which can be solved. With this value of $\text{tr}\mathbf{c}^{n+1}$ we calculate using equation (3.4) the value of all components of \mathbf{c} at the new time level. Finally using (2.7) we obtain the polymer stress at the new time level.

To compute the various viscoelastic flows we use the following procedure. First a computation of the Newtonian fluid is carried out by running the code without the FENE-P model until a steady state is reached. The polymer computations are started with a fully developed velocity field of the Newtonian fluid as initial condition. The initial condition for the conformation tensor \mathbf{c} is computed by substituting the mean velocity profile $U(z)$ for Newtonian flow, which for this initialization is assumed to be a time-independent unidirectional shear flow, in equation (3.2). This is done to develop a not too unrealistic field for \mathbf{c} as starting condition. Initially, the fields of \mathbf{c} and the velocity \mathbf{u} are not coupled (i.e. $\beta = 1$). This is continued until a steady state is reached for \mathbf{c} . From then on the value of β is set to the value given in table 1. The coupled equations (3.1), (3.2) and (2.7) are then integrated until a steady state is again reached, which takes approximately $10\mathcal{T}$, where the time scale \mathcal{T} is defined as H/u_* . The computations are then continued for another $10\mathcal{T}$ – $12\mathcal{T}$ during which data fields are collected with a separation of $0.1\mathcal{T}$. This time separation is large compared to the integral time scale of the turbulence, so that these data fields can be considered as statistically independent. During post-processing these data fields are used to compute various statistics, which are obtained by spatial averaging over the streamwise and spanwise directions and temporal (ensemble) averaging over the data fields.

3.2. Flow parameters

All physical quantities to be discussed in the following sections are expressed in dimensionless wall units denoted with the superscript $+$. This means that all velocities are scaled with the friction velocity u_* and stresses with ρu_*^2 . The wall shear stress τ_w is connected to the pressure gradient via the streamwise momentum balance according to

$$\tau_w = \frac{H}{2} \frac{\Delta P}{\Delta x}. \quad (3.5)$$

All lengths are scaled with $\eta_w/\rho u_*$, with η_w the local viscosity at the wall. We have to specify the viscosity at a fixed position because of the shear-thinning behaviour of the FENE-P model. The viscosity is not constant, but is decreasing with increasing shear rate. The viscosity η_w is defined as in Pinho & Whitelaw (1990), Draad, Kuiken & Nieuwstadt (1998) and Ptasinski *et al.* (2001) by

$$\eta_w = \frac{\tau_w}{(\partial U_x/\partial z)_w}. \quad (3.6)$$

The simulations are performed in a flow box with dimensions $1.5H \times H \times H$ in the streamwise (x), spanwise (y) and wall-normal (z) directions respectively. Turbulent flow in a comparable domain has been studied in detail by Jimenez & Moin (1991), who call it a minimal flow unit (MFU). The concept of the MFU is the creation of a minimal size flow geometry in which essential turbulent characteristics, dynamics and morphology resemble the turbulence properties of a full-scale turbulent channel flow. The idea of using a MFU in our case is that this minimizes the number of grid points needed for computation of the flow field, so that enough computational resources remain for the computation of the polymer stress which is computationally very expensive. It is relevant to point out that our flow is fully turbulent in the whole channel and at all times. Jimenez & Moin (1991) found that the requirements for the MFU are a spanwise extent of at least 100 wall units and a streamwise extent of 250–350 wall units. Because we have to deal with polymer fluids, for which turbulent structures like streaks usually become larger, we have chosen a somewhat bigger domain. Based on the Reynolds number $Re_* = \rho u_* H/\eta = 360$ for which the Newtonian flow simulation is carried out, the dimensions of our channel are chosen as $(L_x, L_y, L_z) = (540x^+, 360y^+, 360z^+)$. According to Dean's correlation (Dean 1978) for the relationship between the wall stress τ_w and the bulk (mean) velocity U_b the Reynolds number for Newtonian flow based on U_b and H is equal to $Re = 5500$. For the viscoelastic cases we define the Reynolds number as

$$Re_w = \frac{\rho U_b H}{\eta_w}. \quad (3.7)$$

The computations are carried out on a grid with $48 \times 32 \times 100$ gridpoints in the x -, y - and z -directions respectively and with a dimensionless time step of $\Delta t = 2 \times 10^{-4} \tilde{t}$ for the Newtonian case. For the viscoelastic cases the time step is set to half this value in order to keep the simulations stable. Our results for Newtonian flow agree very well with the results of Kim, Moin & Moser (1987), which is considered as the standard reference for direct numerical simulations of channel flow at moderate Reynolds numbers.

As we have seen above, we can choose three parameters freely in the FENE-P model: the extensibility parameter b , the relaxation time λ and the ratio of solvent to the total viscosity β . An objective of our study is to investigate how these parameters affect the flow and its drag-reducing capability. Therefore, let us consider these parameters in more detail.

For a system in equilibrium, we can derive from (2.8)–(2.9) (with $\nabla \cdot \mathbf{u} = 0$ and $\partial \mathbf{c} / \partial t = 0$) that

$$\text{tr} \mathbf{c}_{\text{eq}} = \frac{3b}{b+3}, \quad (3.8)$$

Run	β	We_*	b	Re_w	η_w/η_0	%DR
N	1	–	–	5486	1	–
A	0.6	54	100	8609	0.792	26
B	0.6	54	1000	10246	0.938	61
C	0.6	72	1000	10574	0.967	66
D	0.8	54	1000	7020	0.977	40
E	0.4	54	1000	12616	0.810	64

TABLE 1. Numerical parameters of the FENE-P model used in the direct numerical simulations. All simulations are carried out with $Re_* = 360$. N indicates the Newtonian flow simulation.

while for the maximum value $\text{tr}\mathbf{c}_{\max} = b$, so that

$$\sqrt{\frac{\text{tr}\mathbf{c}_{\max}}{\text{tr}\mathbf{c}_{\text{eq}}}} = \sqrt{\frac{b+3}{3}}. \quad (3.9)$$

In other words b determines the ratio of the maximum and the equilibrium polymer length.

The relaxation time λ can be written as a dimensionless Weissenberg number which give the ratio of the relaxation time of the polymers to the characteristic time scale of the flow:

$$We_* = \frac{\lambda}{\eta_0/\rho u_*^2} = \frac{\rho \lambda u_*^2}{\eta_0}. \quad (3.10)$$

We use in the definition of the Weissenberg number the zero-shear-rate viscosity η_0 because of the shear-thinning behaviour of the polymer model. Finally, β is directly related to the polymer concentration via (2.10).

One simulation for Newtonian flow and five simulations for the polymer solutions have been performed. In all simulations the Reynolds number is $Re_* = 360$, but the three parameters of the FENE-P model are varied. An overview of the numerical parameters for which computations have been carried out is given in table 1, where N denotes the Newtonian flow simulation and A, B, C, D and E refer to the viscoelastic cases. Runs A and B differ in the extensibility parameter, i.e. the maximum polymer length with run B being representative of a longer polymer than run A; runs B and C differ with respect to the relaxation time, i.e. the Weissenberg number with run C being representative of a stiffer polymer than run B; the difference between runs B, D and E is the parameter β , i.e. the polymer concentration n , with increasing polymer concentrations going from runs D, B to E. The value of β , especially for run E, might seem to be low (i.e. high polymer concentration) compared to other studies like Sureshkumar *et al.* (1997). However, we consider these values to be realistic as the polymer solutions in most high-regime drag-reduction experiments (Warholic *et al.* 1999a; Ptasinski *et al.* 2001) show very significant shear-thinning behaviour which implies non-negligible effects of the polymer on the fluid properties.

The results of these computations will be compared with each other and with the results of the Newtonian simulation. In addition we will compare the results for a set of experiments that we have carried out and which are described in detail in Ptasinski *et al.* (2001). From these experiments four cases have been selected, for which drag reduction is close to the simulations. They are denoted with the abbreviation ‘exp’ and the same letter as the corresponding simulation. For completeness, an overview of the corresponding simulations and experiments is presented in table 2.

Simulations		Experiments		
Run	%DR	Run	Concentration	%DR
N	–	exp N	none (water)	–
A	26	exp A	20 w.p.p.m.	23
B	61	exp B	103 w.p.p.m.	63
C	66	exp C	435 w.p.p.m.	70

TABLE 2. Overview of the simulations (see table 1) and corresponding experiments (see Ptasinski *et al.* 2001) which are used in the comparison of the results.

4. Flow statistics

4.1. Relation between friction factor and Reynolds number

Usually the amount of drag reduction (as a percentage) is expressed as the reduction of the pressure drop (or alternatively as the reduction of the friction coefficient) due to the addition of the polymers compared to Newtonian flow (see Gyr & Bewersdorff 1995):

$$DR\% = \frac{\Delta P_N - \Delta P_P}{\Delta P_N} \times 100\% = \frac{C_{F,N} - C_{F,P}}{C_{F,N}} \times 100\% \quad (4.1)$$

at equal (wall) Reynolds number for the polymer and Newtonian fluid. In this equation C_F is the friction coefficient and the suffices N and P stand for the Newtonian and polymer case, respectively. The friction coefficient is defined as

$$C_F = \frac{\tau_w}{\frac{1}{2}\rho U_b^2}, \quad (4.2)$$

where τ_w is the wall shear stress and U_b the bulk or mean velocity. For a Newtonian fluid the relation between the friction coefficient and the Reynolds number for a laminar and turbulent flow is given by Dean (1978):

$$C_F = \frac{12}{Re} \quad (4.3)$$

and

$$C_F = 0.073Re^{-1/4}, \quad (4.4)$$

where the Reynolds number is defined in terms of the channel height H and the bulk velocity U_b . Note that due to the general similarity between pipe and channel flow (4.4) is very similar to Blasius' relation for pipe flow (with the only difference being that the value of the constant is 0.079 instead of 0.073). When polymers are added the drag in turbulent flow will be lower (at least if the onset Reynolds number is exceeded). At high polymer concentrations the friction coefficient will approach an empirical asymptote, called the maximum drag reduction asymptote (MDR) or Virk (1975) asymptote which is

$$C_F^{-1/2} = 19.0 \log(Re_w C_F^{1/2}) - 32.4. \quad (4.5)$$

This relation was originally proposed for pipe flow, but we will show in the next section that it is also applicable to channel flow. Re_w is the wall Reynolds number defined in (3.7).

The relation between the friction factor C_F and the wall Reynolds number Re_w is shown in figure 1. Let us first consider the results of the numerical simulations.

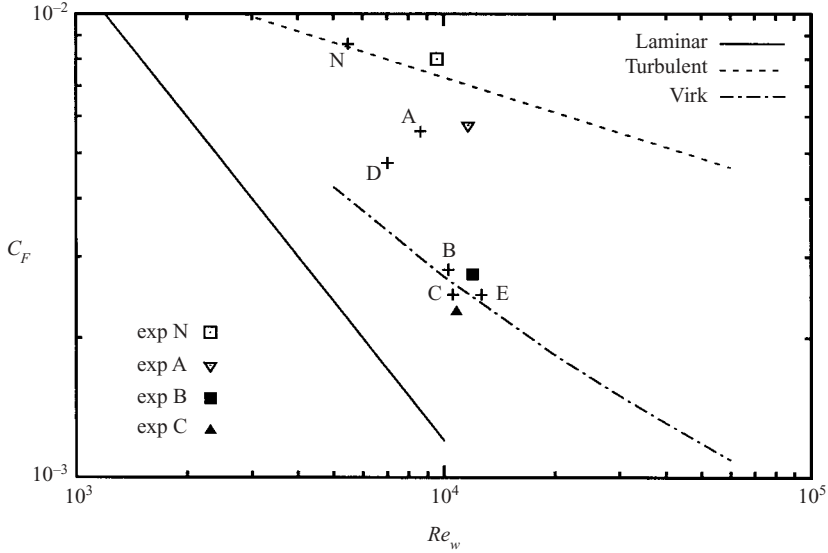


FIGURE 1. The relation between the friction coefficient and the wall Reynolds number. The + symbols marked by the letters N, A, B, C, D and E are the results of the numerical simulations for which the details are given in table 1. The other symbols denote experiments and each experimental is marked by a letter to indicate the 'closest' simulation. The three lines are for (4.3), (4.4), and (4.5).

For a relatively small value of the extensibility parameter ($b = 100$, run A) we find only a small amount of drag reduction. On increasing this parameter (to $b = 1000$, run B) the drag reduction increases to a value close to the maximum drag reduction asymptote. When we further increase the elasticity (to $We_s = 72$, run C) or the polymer concentration (to $\beta = 0.4$, run E) the results remain near the asymptote. A smaller value of the concentration ($\beta = 0.8$, run D) leads to a smaller value of the drag reduction. Let us next compare these results with LDV experiments on turbulent pipe flow. For details regarding these experiments refer to den Toonder *et al.* (1997) and Ptasiński *et al.* (2001). Four cases have been selected, in which the value of the drag reduction is comparable with the simulations N (Newtonian), A, B and C. The drag reduction percentages for the experiments are: for exp A: %DR = 23, for exp B: %DR = 63 and for exp C: %DR = 70 and these data are also plotted on figure 1. The statistical errors for the LDV experiments are approximately 2% for the first moments (mean velocity) and 4% for the second moments (r.m.s. values and stresses).

4.2. Velocity statistics

4.2.1. Mean velocity

It is known that the mean streamwise velocity profile for fully developed turbulence at large Reynolds numbers obeys the following relations in the viscous sublayer and in the logarithmic layer, respectively (see Kim *et al.* 1987):

$$U^+ = z^+, \quad z^+ < 5, \quad (4.6)$$

$$U^+ = 2.5 \ln(z^+) + 5.0, \quad z^+ > 30. \quad (4.7)$$

In figures 2(a), 2(b) and 2(c) we show the results for the dimensionless mean streamwise velocity profile as function of the distance from the wall z^+ for the Newtonian flow and for the viscoelastic cases together with the expressions given

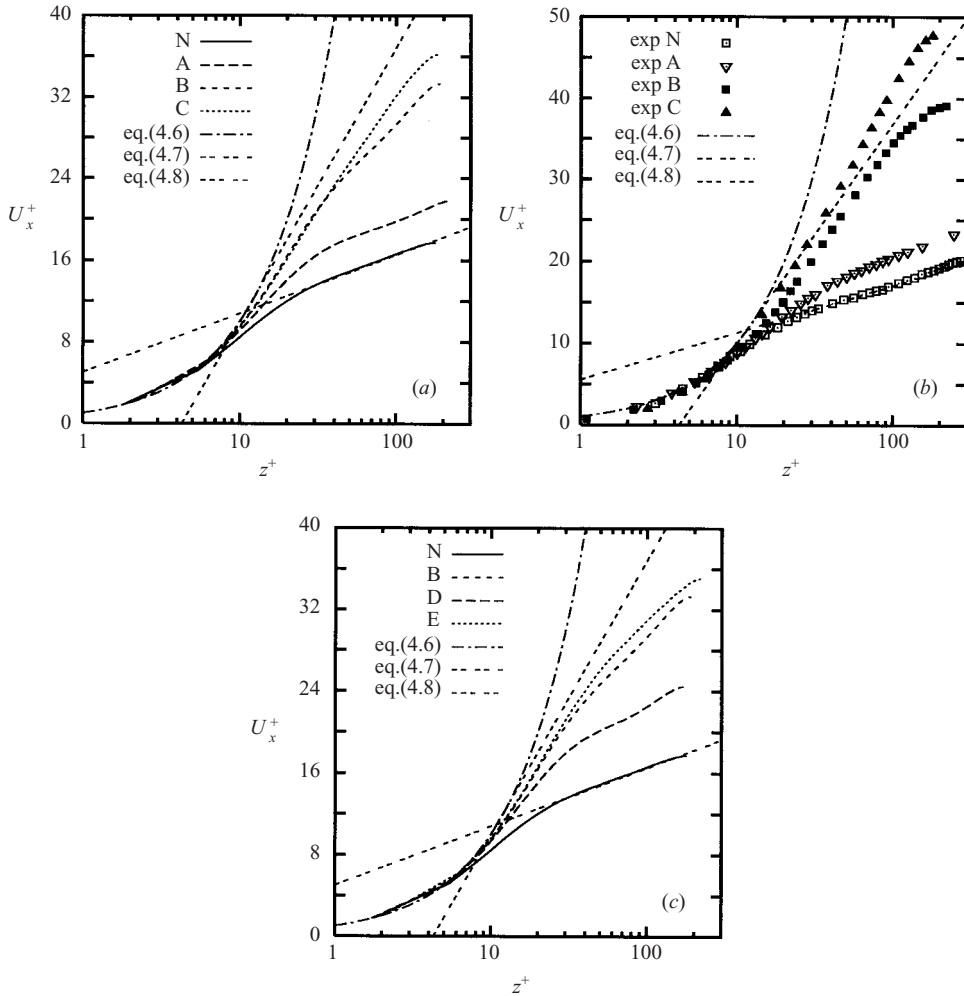


FIGURE 2. Mean streamwise velocity profile as a function of the distance from the wall z^+ . (a) DNS of Newtonian profile and runs A, B and C. (b) Experiments from Ptasinski *et al.* (2001) for cases comparable with the DNS cases N, A, B and C. (c) DNS of Newtonian profile and runs B, D and E. Also shown are the theoretical profiles in the viscous sublayer (4.6), the logarithmic layer for Newtonian flow (4.7) and the Virk asymptote (4.8).

above. In the viscous sublayer all profiles collapse to (4.6) by definition. Further away from the wall the velocity of the polymeric flow increases compared to Newtonian case, which is consistent with drag reduction. Virk *et al.* (1970) and Virk (1975) have proposed that for the maximum drag reduction asymptote the velocity profile should satisfy

$$U^+ = 11.7 \ln(z^+) - 17.0, \quad z^+ > 30. \quad (4.8)$$

Originally this profile was proposed for pipe flow. However Warholic *et al.* (1999*a,b*, 2001) established in their experimental (LDA and PIV) work that this profile is also valid for a channel flow.

The profile for the Newtonian fluid is in excellent agreement with (4.6) in the viscous sublayer and with (4.7) in the logarithmic layer, both for the simulations and for the experiments. In figure 2(a) we see that for $b = 100$ (case A) the profile

in the logarithmic layer is shifted upwards parallel to the logarithmic profile of the Newtonian simulation. This implies that the additive constant in (4.7) is increased from 5.0 to 8.4. The same behaviour is seen in the experimental results for low drag reduction (case exp A) shown in figure 2(b). In the channel flow experiments of Warholic *et al.* (1999a) and in the DNS of Sureshkumar *et al.* (1997) the same behaviour is found for the mean velocity profile at low drag reduction. Furthermore, the upward shift of the logarithmic profile can be interpreted as a thickening of the buffer layer. According to Lumley (1969, 1973) the upward shift of the logarithmic profile is equivalent to drag reduction.

For the simulations with higher drag reduction, which are mainly connected to an increase of the elongational parameter b (runs B, C, D and E) the slope of the logarithmic profile deviates from the value given by (4.7). For the cases with the highest drag reduction (C and E) the slope is close to the value given by the maximum drag reduction asymptote (4.8). To our knowledge this is the first simulation in which the maximum drag reduction asymptote has been confirmed. Other simulations, e.g. Dimitropoulos *et al.* (1998), had either a too low value of the Reynolds number or a too high value of β , i.e. a too low polymer concentration. The experimental cases B and C in figure 2(b) show a profile close to the maximum drag reduction profile. This is consistent with the results of the simulations for the comparable cases. The maximum drag reduction profile is even slightly exceeded for case C, which can be attributed to very strong shear-thinning behaviour of the fluid for this case and therefore some inaccuracies in determination of the viscosity at the wall and the scaling in terms of the wall units.

The effect of the viscosity ratio (and thus of the polymer concentration) is illustrated in figure 2(c), where it is shown that for the lowest values of β (runs B and E) a limit for the slope close to the maximum drag reduction profile is reached, while for a lower viscosity ratio (run D) only a minor increase of the slope compared to the Newtonian profile is found.

Finally we should mention that for the cases with small values of b (not shown in this paper) we have found only a minor effect on the velocity profile compared to Newtonian flow. Summarizing, we have seen that a high extensibility parameter b in combination with high elasticity given by large values of We_* and large values of the polymer concentration or alternatively low values of β are necessary to reach the maximum drag reduction regime.

4.2.2. Second-order turbulence statistics

We introduce the well-known Reynolds decomposition for a fluctuating variable by splitting this into a mean part (denoted by upper case) and a fluctuation (denoted by lower case with a prime). Alternatively we indicate the mean part by an overbar (...). The dimensionless root mean square (r.m.s.) of the velocity fluctuations in the α -direction ($\alpha = (x, y, z)$) is defined as

$$\text{rms}(u_\alpha^+) = \frac{1}{u_*} \sqrt{u_\alpha'^2}. \quad (4.9)$$

The root mean square of the streamwise velocity fluctuations, $\text{rms}(u^+)$ is shown in figure 3 for both simulations and experiments. The results of figure 3(a) indicate that the peak value for the polymer solutions is higher than that for the Newtonian case. The peak value seems to grow with increasing extensibility parameter b (compare for instance runs A and B). However, for the case of the highest Weissenberg number (run C, for which the largest drag reduction is observed) the value is decreased

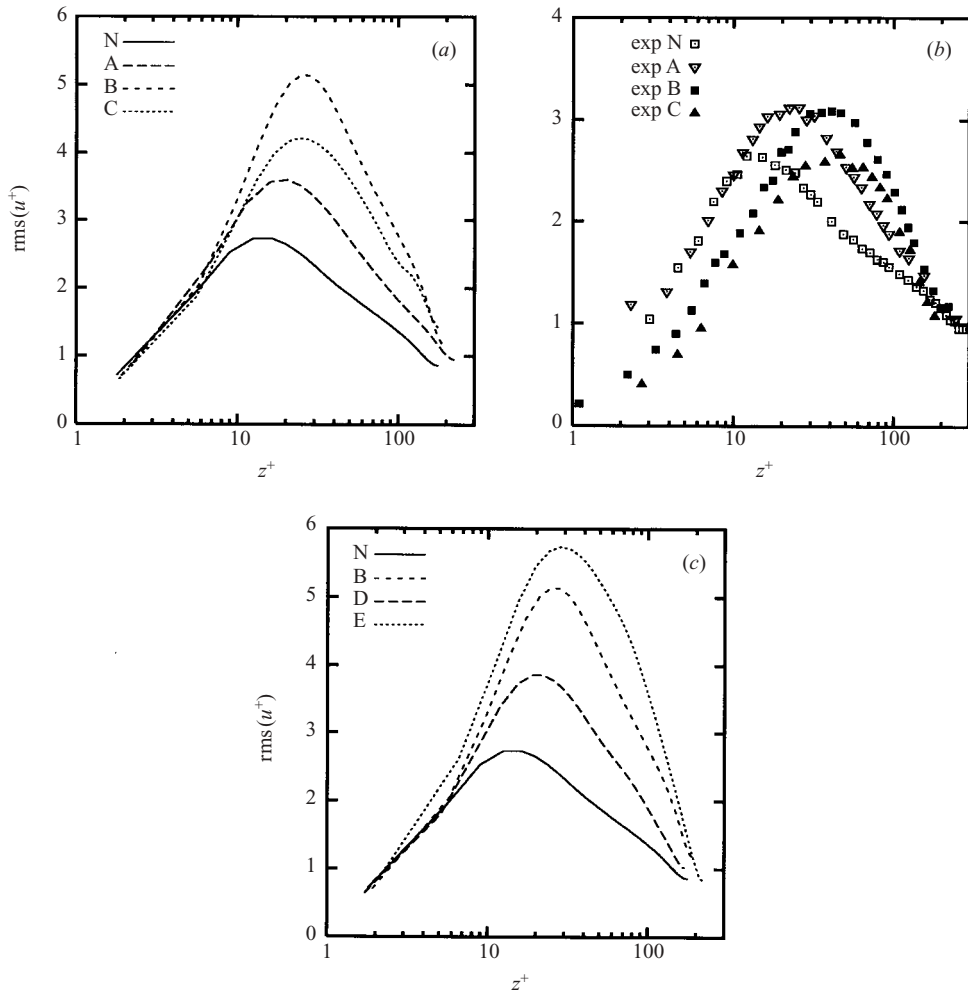


FIGURE 3. Profiles of the root mean square of the streamwise velocity fluctuations as a function of the distance from the wall. (a) DNS of Newtonian profile and runs A, B and C. (b) Experiments from Ptasinski *et al.* (2001) with cases comparable with the DNS cases N, A, B and C. (c) DNS of Newtonian profile and runs B, D and E.

compared to case B. This behaviour of the peak value (including the decrease at the highest drag reduction) is confirmed by the experiments shown in figure 3(b). However, it appears that the height of the peak found in the simulations (especially in the high drag reduction runs) is higher than the peak value observed in the experiments. This might be due to shortcomings in the FENE-P model. Brownian dynamics simulations of FENE (without pre-averaging) and FENE-P (with pre-averaging) dumbbells (Herrchen & Öttinger 1997; Keunings 1997) and chains (Van den Brule 1993) in non-stationary elongational flows show for instance that the Peterlin approximation can cause some changes in the rheological behaviour (like overprediction of the polymer stresses). In this respect we note that the difference between simulations and experiments occurs in the region where the highest elongation occurs, i.e. in the buffer layer.

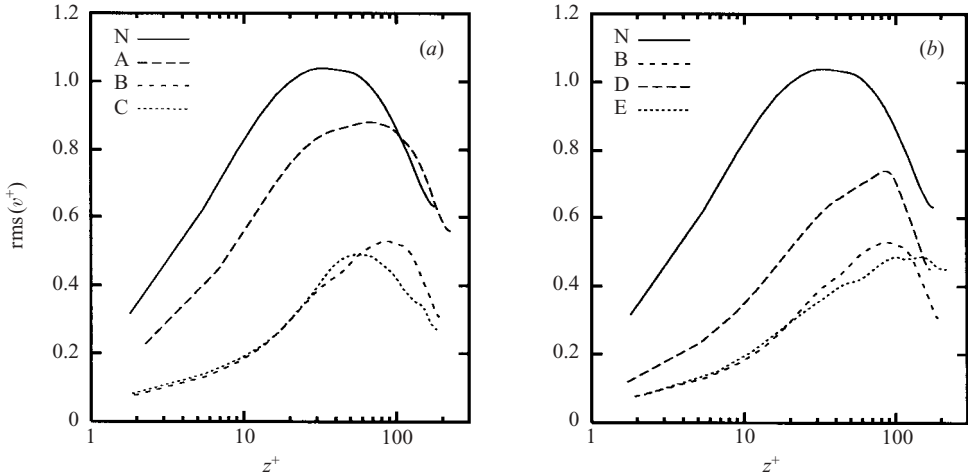


FIGURE 4. Profiles of the root mean square of the spanwise velocity fluctuations as a function of the distance from the wall. (a) DNS of Newtonian profile and runs A, B and C. (b) DNS of Newtonian profile and runs B, D and E.

Figure 3(a) also shows that for the polymer cases the location of the peak is shifted to the centre of the channel. This is consistent with the shift of the logarithmic region in the mean velocity profile. Again this behaviour is consistent with the experiments of figure 3(b). Finally, we note that close to the wall (for $z^+ < 10$) and in the centre of the channel (for $z^+ > 100$) the value of $rms(u^+)$ for the polymeric flows does not differ much from the Newtonian case.

In figure 3(c) we show the behaviour for the cases with varying viscosity ratio β or for varying polymer concentration. We see that the peak of the r.m.s. value increases monotonically with decreasing β . Also, the location of the peak moves continuously away from the wall with decreasing β .

In figure 4 we present the root mean square of the spanwise velocity fluctuations, $rms(v^+)$, as a function of the distance from the wall. In figure 4(a) we observe for $b = 100$ (case A) a slight decrease compared to the Newtonian case with again a shift of the peak to the centre of the channel. The values in the centre of the channel are comparable to those for the Newtonian flow. For the large value of b (run B) we observe a strong decrease across the whole channel. Also, a larger shift of the peak value is noted. For high elasticity (run C) the values do not alter significantly compared to those of run B except near the centre of the channel. The effect of varying the concentration shown in figure 4(b) indicates a general decrease of $rms(v^+)$ for increasing polymer concentration, i.e. decreasing β , although only a minor difference is found between the two highest concentrations. The overall behaviour found for $rms(v^+)$ is in reasonable agreement with experiments of Pinho & Whitelaw (1990), who are among the few who measured spanwise velocity fluctuations.

The r.m.s. of the wall-normal velocity fluctuations, $rms(w^+)$, is shown in figure 5 for both the simulations and the experiments. The results of the simulations show an almost continuous decrease across the channel for the runs A, B and C or in other words for increasing drag reduction. Similarly to the spanwise r.m.s. the values decrease with increasing polymer extensibility and decrease only slightly with increasing elasticity (figure 5a). The experiments shown in figure 5(b) confirm the

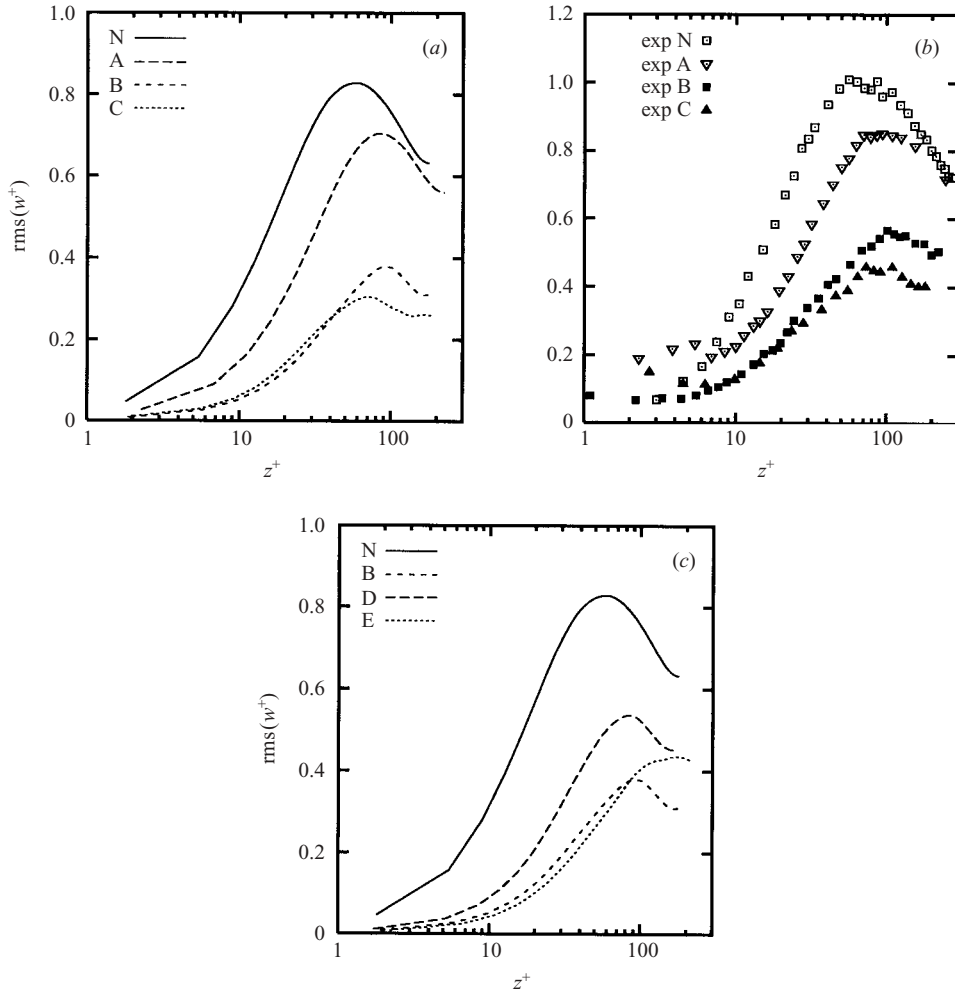


FIGURE 5. Profiles of the root mean square of the wall-normal velocity fluctuations as a function of the distance from the wall. (a) DNS of Newtonian profile and runs A, B and C. (b) Experiments from Ptasinski *et al.* (2001) with cases comparable with the DNS cases N, A, B and C. (c) DNS of Newtonian profile and runs B, D and E.

behaviour of $\text{rms}(w^+)$ as function of the drag reduction. The agreement between simulation and experimental results is very good, at least qualitatively.

In both the simulations and experiments we observe again a shift of the peak value of $\text{rms}(w^+)$ towards the centre of the channel. The effect of polymer concentration in figure 5(c) shows an overall decrease as a function of increasing concentration, i.e. decreasing β , except for the two highest concentrations where the change is minimal.

4.3. Mean polymer extension

In some explanations of drag reduction (Lumley 1969, 1973) the influence of the polymers on the turbulent flow is connected to the extension of the polymers by the flow deformation. This would for instance result in a high extensional viscosity, which could possibly affect the turbulent structures. Therefore we consider the mean extension of the polymers, i.e. the polymer length compared to the equilibrium length

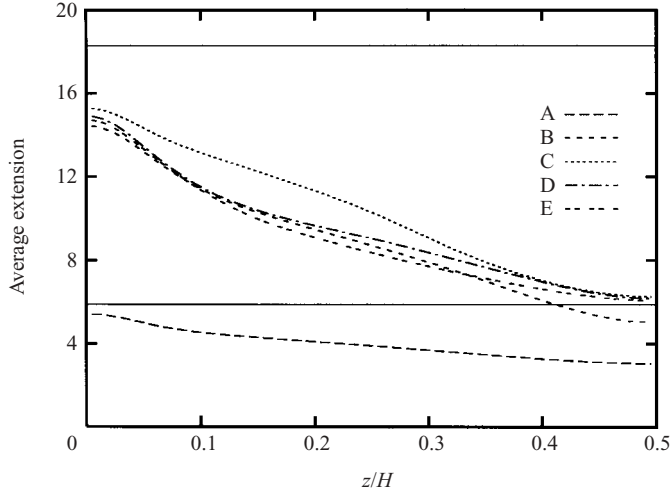


FIGURE 6. The average polymer extension for the simulations of the viscoelastic fluids. The two continuous lines denote the theoretical maximum values, see (3.9), for run A with $b = 100$ (lower line) and runs B, C, D and E with $b = 1000$ (upper line).

as a function of the position in the flow. The polymer extension is normalized to the length in equilibrium in order to show how much the polymers are stretched in the turbulent flow. The dimensionless length of the polymers is by definition equal to $\sqrt{\text{tr}\mathbf{c}} = |\langle \tilde{\mathbf{Q}} \tilde{\mathbf{Q}} \rangle|$. We have seen before that the maximum length is given by $\sqrt{\text{tr}\mathbf{c}_{\text{max}}} = \sqrt{b}$ and that the ratio between the maximum and the equilibrium length is given by (3.9). This equation implies for instance that for $b = 1000$ (cases B, C, D and E) the polymer can extend to about 18 times its equilibrium length. In figure 6 the mean polymer extension is shown as a function of the distance to the wall. We see that for smallest value of the extensibility parameter b , i.e. $b = 100$ or (case A), the extension is relatively small, which corresponds to a small amount of drag reduction. Nevertheless in relative terms, compared to their maximum value the polymers for case A are close to fully extended near the wall.

For $b = 1000$, i.e. cases B, C, D and E, we find much greater stretching of the polymers, again primarily in the wall region. Therefore we conclude that a sufficiently high value of the extensibility parameter is essential for drag reduction. Figure 6 also shows that the highest value of the Weissenberg number (case C) results in the largest extension. This case also corresponds to highest drag reduction. Compared to their maximum value the cases with $b = 1000$ do not seem to reach a fully extended state.

4.4. Turbulent, viscous and polymer shear stresses

For a stationary fully developed flow we can derive from (3.1) an equation for the mean flow which results in a balance between the pressure gradient and the total stress. Together with the stress decomposition into a solvent and a polymer part, and with the Reynolds decomposition the equation for the xz -component of the shear stress becomes

$$0 = -\frac{\partial P}{\partial x} + \frac{\partial}{\partial z} \left(\underbrace{-\overline{u'_x u'_z} + \frac{\beta}{Re_*} \frac{\partial U_x}{\partial z} + \overline{\tau_{xz}^{(p)}}}_{\overline{\tau}^+} \right), \quad (4.10)$$

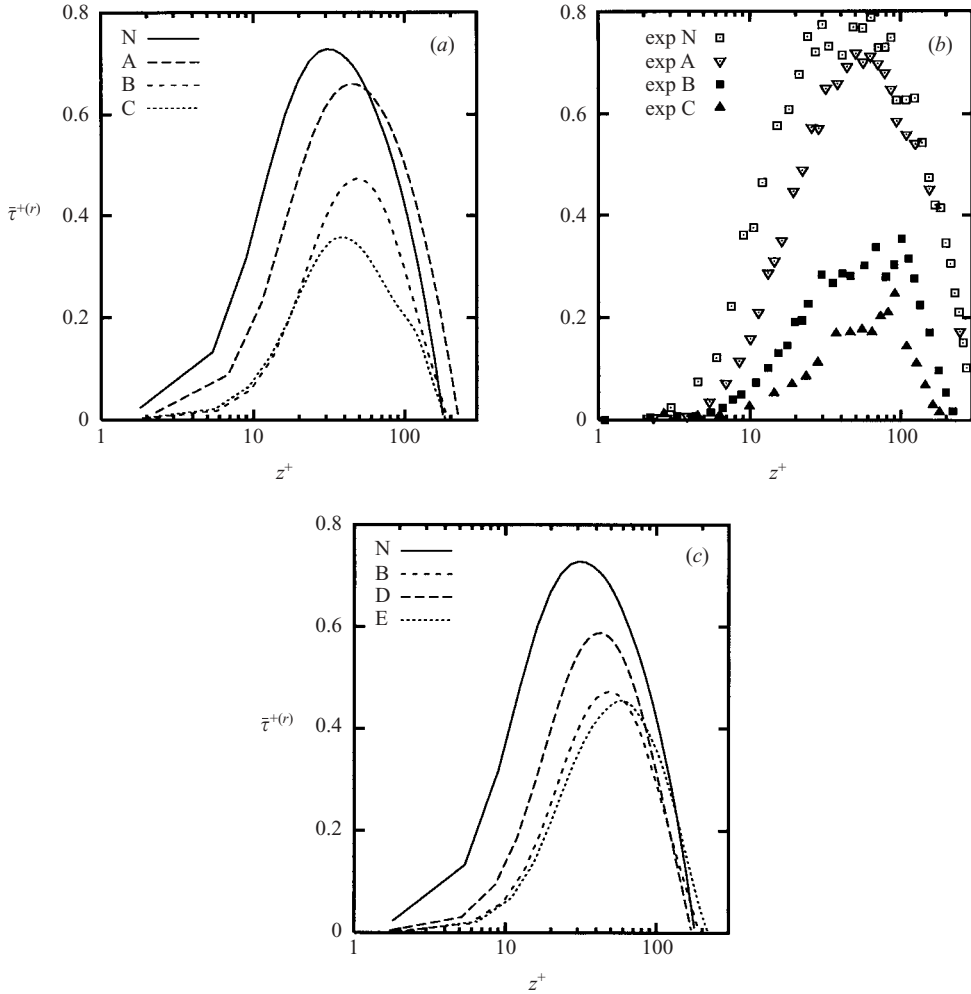


FIGURE 7. Profiles of the turbulent (Reynolds) shear stress as function of the distance from the wall. (a) DNS of Newtonian profile and runs A, B and C. (b) Experiments from Ptasinski *et al.* (2001) with cases comparable with the DNS cases N, A, B and C. (c) DNS of Newtonian profile and runs B, D and E.

with $\bar{\tau}^+ = \bar{\tau}^{+(r)} + \bar{\tau}^{+(s)} + \bar{\tau}^{+(p)}$ indicating the turbulent or Reynolds stress, the viscous stress of the solvent and the polymer stress, respectively. The sum of these three contributions is the total shear stress which, because of the constant pressure gradient, has a linear profile over the channel height with the value zero at the centre of the channel and the value $\pm\tau_w$ given by (3.5) at the walls. The total shear stress is thus equal to $\bar{\tau}^+ = 1 - 2z/H$.

Let us first discuss the turbulent stress obtained from our simulations and from experiments. The results are presented in figure 7. All viscoelastic simulations result in a shift away from the wall and a decrease in the magnitude compared to the Newtonian simulation. The decrease becomes larger for increasing polymer extensibility, elasticity and concentration. The general behaviour is confirmed by the experiments shown in figure 7(b) and also by other experiments (see e.g. Harder & Tiederman 1991; Wei & Willmarth 1992). The strongest reduction in the stress found in our simulations

for run C is about 50%. This is less than observed in our experimental work (see figure 7c), which results in a reduction of dimensionless Reynolds stress by about 75%. Nevertheless the trend found in our simulations is confirmed by the experiments. Warholic *et al.* (1999a, b) suggest that at maximum drag reduction the Reynolds stress should nearly vanish. Neither our simulations nor our observations of figure 7 confirm this suggestion.

The various contributions to the total shear stress as given by (4.10) obtained from our simulations are shown in figure 8. All values are presented in dimensionless form (scaled with ρu_*^2). For reasons of simplicity we show only half of the domain and depict all stresses as positive quantities. For Newtonian flow (figure 8a) only the Reynolds stress and the viscous stress are non-zero and they add up to the total stress. For the viscoelastic simulations (figure 8b–f) all three contributions are plotted ($\bar{\tau}^{+(r)}$, $\bar{\tau}^{+(s)}$, $\bar{\tau}^{+(p)}$) and these are directly computed from simulations. The most obvious result from these latter plots is that for the viscoelastic simulations the Reynolds and viscous stresses no longer add up to the total stress. This is called the ‘Reynolds stress deficit’. It implies that there must be a contribution of the polymers to the stress. For the low drag reduction simulations (figures 8b and 8e) the polymer stress contribution is relatively small and it occurs mainly close to the wall. For the drag reduction close to maximum (figures 8c, 8d and 8f) this contribution is large and can become 40%–50% of the total stress. Moreover, in this case the polymeric stress is important across the whole channel.

The various stress contribution obtained from the experiments are shown in figure 9. In contrast to the simulations the polymer stress in this case is computed indirectly as the difference between the total stress and the sum of the Reynolds and solvent stress. It is clear that the polymer stress increases monotonically with increasing drag reduction and for the highest case (exp C, figure 9d) it contributes 60% of the total stress. This is even more than found in our DNS and is mainly due to the strong Reynolds stress reduction.

5. Energy budgets

In this section we will consider the various terms in the budget of the kinetic energy of the turbulence and in the budget of the elastic energy of the polymers. We use the index notation and apply the well-known summation convention (which means that a repeated index indicates a summation over all coordinate directions).

5.1. Kinetic energy of the mean flow

We first consider the kinetic energy of the mean flow defined by $\frac{1}{2}U_i U_i$. An equation for this quantity is found by multiplying the mean part of the momentum equation (3.1) with U_i . The result is

$$\frac{D}{Dt} \left(\frac{1}{2} U_i U_i \right) = P_u + T_u^{(r)} + T_u^{(s)} + T_u^{(p)} + D_u - \epsilon_u - W_u \quad (5.1)$$

with

$$P_u = -U_i \frac{\partial P}{\partial x_i}, \quad (5.2)$$

$$T_{ii}^{(r)} + T_{ii}^{(s)} + T_{ii}^{(p)} = \frac{\partial}{\partial x_j} \left(-U_i \overline{u'_i u'_j} + \frac{\beta}{Re_*} U_i \frac{\partial U_i}{\partial x_j} + U_i \bar{\tau}_{ij}^{(p)} \right), \quad (5.3)$$

$$D_u = \overline{u'_i u'_j} \frac{\partial U_i}{\partial x_j}, \quad (5.4)$$

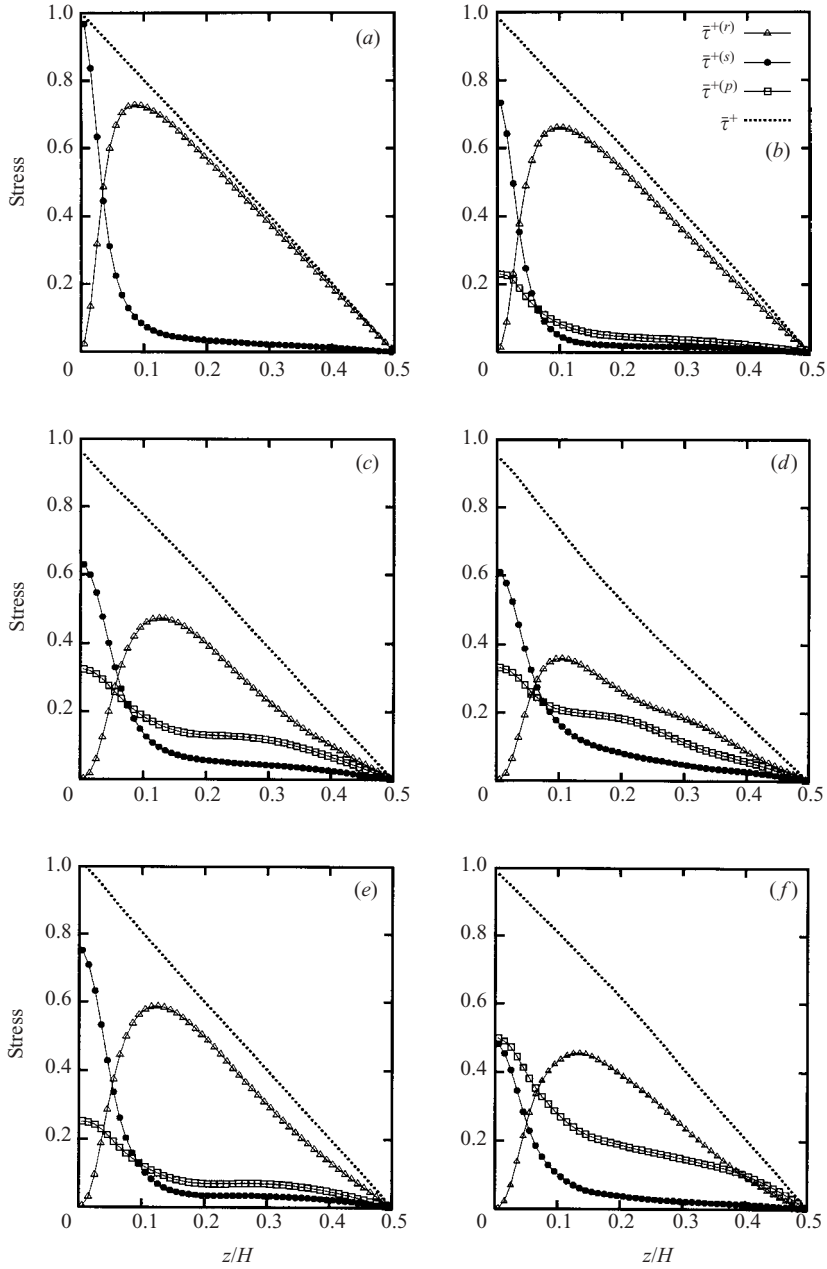


FIGURE 8. Shear stress contributions as a function of the distance from the wall computed with DNS. $\bar{\tau}^{+(r)}$: Reynolds stress, $\bar{\tau}^{+(s)}$: solvent stress, $\bar{\tau}^{+(p)}$: polymer stress, $\bar{\tau}^+$: total stress. (a) Newtonian run; (b) run A; (c) run B; (d) run C; (e) run D; (f) run E.

$$\epsilon_u = \frac{\beta}{Re_*} \left(\frac{\partial U_i}{\partial x_j} \right)^2, \quad (5.5)$$

$$W_u = \bar{\tau}_{ij}^{(p)} \frac{\partial U_i}{\partial x_j}. \quad (5.6)$$

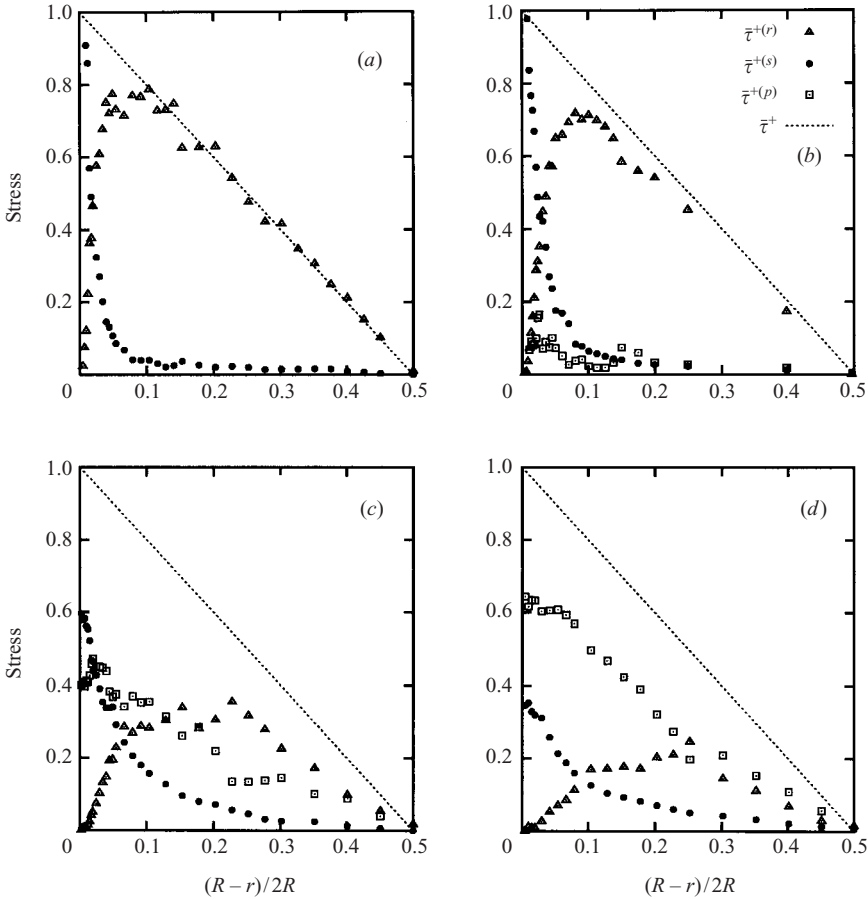


FIGURE 9. Shear stress contributions as a function of the distance from the wall from experiments of Ptasinski *et al.* (2001) with cases comparable with the DNS cases N, A, B and C. $\bar{\tau}^{+(r)}$: Reynolds stress, $\bar{\tau}^{+(s)}$: solvent stress, $\bar{\tau}^{+(p)}$: polymer stress, $\bar{\tau}^+$: total stress. (a) exp N; (b) exp A; (c) exp B; (d) exp C.

In these equations, P_u is the production of mean flow kinetic energy, i.e. the work performed by the mean pressure gradient. The terms $T_u^{(r)} + T_u^{(s)} + T_u^{(p)}$ denote the transport of mean kinetic energy by turbulent velocity fluctuations, by viscous stress and by polymer stress, respectively. When integrated over the entire channel, these three terms will not contribute to the total budget. D_u is called the deformation work. Finally, ϵ_u and W_u stand for dissipation of energy by the Newtonian shear stress and by mean polymer stress, respectively. The production of energy is positive, while the deformation work and the dissipation terms make a negative contribution to the budget.

5.2. Kinetic energy of the turbulence

The equation for the turbulent kinetic energy, $\frac{1}{2}\overline{u'_i u'_i}$ follows by multiplying the equation for the velocity fluctuation with u'_i where the latter equation can be obtained from (3.1). The results is

$$\frac{D}{Dt} \left(\frac{1}{2} \overline{u'_i u'_i} \right) = P_{ii} + T_{ii}^{(r)} + T_{ii}^{(\pi)} + T_{ii}^{(s)} + T_{ii}^{(p)} - \epsilon_{ii} - W_{ii}, \tag{5.7}$$

with

$$P_{ii} = -\overline{u'_i u'_j} \frac{\partial U_i}{\partial x_j}, \quad (5.8)$$

$$T_{ii}^{(r)} = \frac{\partial}{\partial x_j} \left(-\frac{1}{2} \overline{u'_i u'_j u'_j} \right), \quad (5.9)$$

$$T_{ii}^{(\pi)} = \frac{\partial}{\partial x_j} \left(-\overline{u'_i p'} \delta_{ij} \right), \quad (5.10)$$

$$T_{ii}^{(s)} = \frac{\partial}{\partial x_j} \left(\frac{1}{2} \frac{\beta}{Re_*} \frac{\partial}{\partial x_j} \overline{u'_i u'_i} \right), \quad (5.11)$$

$$T_{ii}^{(p)} = \frac{\partial}{\partial x_j} \left(\overline{u'_i \tau'_{ij}{}^{(p)}} \right), \quad (5.12)$$

$$\epsilon_{ii} = \frac{\beta}{Re_*} \left(\frac{\partial u'_i}{\partial x_j} \right)^2, \quad (5.13)$$

$$W_{ii} = \overline{\tau'_{ij}{}^{(p)} \frac{\partial u'_i}{\partial x_j}}. \quad (5.14)$$

Here, P_{ii} is the production of turbulent kinetic energy and we note that $P_{ii} = -D_u$ so that this term will be always positive. $T_{ii}^{(r)}$, $T_{ii}^{(\pi)}$, $T_{ii}^{(s)}$ and $T_{ii}^{(p)}$ are transport terms, defining energy transport by the fluctuating Reynolds stress, by pressure fluctuations, by the fluctuating viscous stress and by fluctuating polymer stresses, respectively. Again, when integrated over the channel height these transport terms will not contribute to the budget. The viscous dissipation ϵ_{ii} will always be a loss term and the polymer stress work W_{ii} can in principal be either positive or negative. All energy budget terms are made dimensionless consistent with the scaling of the velocity statistics in §4.2.

We consider here the results for the turbulent kinetic energy for Newtonian flow and for two polymer simulations: runs A ($b=100$) and B ($b=1000$), both with $\beta=0.6$ and $We_* = 54$. In figures 10 and 11 the various terms in the turbulent kinetic energy budget terms are plotted as a function of the distance from the wall. The results for Newtonian flow are in very good agreement with data from Mansour, Kim & Moin (1988). For viscoelastic flow we observe a decrease of the production with increasing extensibility parameter. For the highest value of b we observe a significant shift of the peak away from the wall, which is consistent with the thickening of the buffer layer. The viscous dissipation for the polymer flows is much smaller than for the Newtonian flow. Finally, we see that the polymer stress work makes a negative contribution to the budget everywhere in the channel, which means this is acting as a dissipative term. The polymer stress work becomes more important with increasing b . The contributions of the transport terms illustrated in figure 11 show a similar behaviour: all budget terms (for turbulent, viscous and polymer transport) become smaller in magnitude with increasing b and show a significant shift away from the wall.

5.3. Turbulent kinetic energy per component

Let us now consider the equations for the various components of the turbulent kinetic energy, $\frac{1}{2} \overline{u'_\alpha u'_\alpha}$, separately. The balance equation for the α -component is (no summation

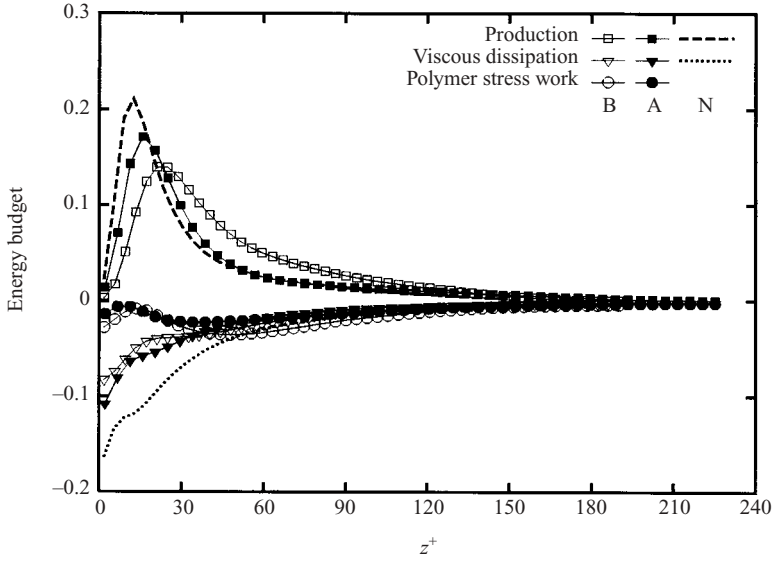


FIGURE 10. Turbulent kinetic energy budgets as a function of the distance from the wall z^+ for Newtonian flow (thick lines) and for the FENE-P model with $\beta=0.6$, $We_* = 54$ and $b=100$ (run A, closed symbols) and $b=1000$ (run B, open symbols). Plotted are the lines for production (P_{ii}), viscous dissipation ($-\epsilon_{ii}$) and polymer stress work ($-W_{ii}$).

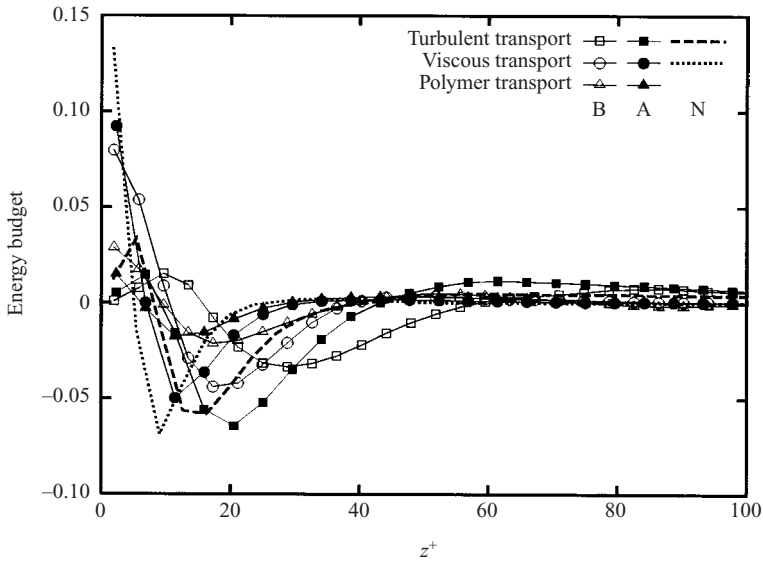


FIGURE 11. Turbulent kinetic energy budgets as a function of the distance from the wall z^+ for Newtonian flow (thick lines) and for the FENE-P model with $\beta=0.6$, $We_* = 54$ and $b=100$ (run A, closed symbols) and $b=1000$ (run B, open symbols). Plotted are the lines for transport by turbulent stress ($T_{ii}^{(r)}$), viscous (solvent) stress ($T_{ii}^{(s)}$) and polymer stress ($T_{ii}^{(p)}$). The transport by pressure fluctuations ($T_{ii}^{(\pi)}$) is very small and is not shown in this graph. Only $z^+ < 100$ is shown as all transport terms are almost zero in the centre of the channel.

over α)

$$\frac{D}{Dt} \left(\frac{1}{2} \overline{u'_\alpha u'_\alpha} \right) = P_{\alpha\alpha} + T_{\alpha\alpha}^{(r)} + T_{\alpha\alpha}^{(\pi)} + T_{\alpha\alpha}^{(s)} + T_{\alpha\alpha}^{(p)} + \Pi_{\alpha\alpha} - \epsilon_{\alpha\alpha} - W_{\alpha\alpha}, \quad (5.15)$$

with all budget terms defined as in equations (5.8)–(5.14). However, one extra term appears in (5.15), which is called the pressure strain $\Pi_{\alpha\alpha}$ and which is defined[†]

$$\Pi_{\alpha\alpha} = p' \frac{\partial u'_\alpha}{\partial x_\alpha}. \quad (5.16)$$

This term is responsible for redistribution of energy over the three coordinate directions and the sum of the three pressure strain components must be zero.

In figure 12 the terms in the kinetic energy budget for the streamwise component are shown, which is the largest component in magnitude. The production in this budget is equal to the production of the total kinetic energy. For the viscous dissipation there is not much difference with the total energy. The most important result of these graphs is the very strong decrease of the pressure strain for the polymer cases in comparison the Newtonian case. This means that the energy transfer from the streamwise component to the other components is much smaller than for a Newtonian flow and thus that most kinetic energy remains in the streamwise direction. This explains why the r.m.s. of the streamwise velocity fluctuations increases when polymers are added (figure 3a) and why the r.m.s. values of the spanwise and wall-normal fluctuations decrease (figures 4a and 5a). Looking at the polymer stress work, we see that this term is dissipative everywhere in the channel. Unlike the viscous dissipation, the largest (absolute) value is not found at the wall but in the buffer layer. This confirms our hypothesis that the buffer layer is the the region where polymers contribute most to the changes in turbulence. The transport contributions to the energy budget of the streamwise component do not significantly differ from the budget of the total kinetic energy.

The terms of the budget for the spanwise direction are shown in figure 13. Again we find a decrease in magnitude for the pressure-strain term with increasing b which is the only positive contribution to this budget (apart from small transport contributions). The decrease of this term is consistent with the smaller r.m.s. values of the spanwise velocity fluctuations (see figure 4a). Furthermore, for the highest value of b we observe a strong decrease of viscous dissipation which implies that most dissipation is due to the polymers. Note also that the transport terms over the channel height have almost vanished for the highest drag reduction case.

The results for the wall-normal energy budget, given in figure 14 show a similar behaviour to that for the spanwise component. Again we observe a smaller pressure strain with increasing polymer extensibility (and drag reduction), corresponding to smaller r.m.s. (figure 5a). The main dissipation is again due to the polymers.

5.4. Elastic energy of the polymers

Another form of energy which plays a role in our problem is the potential energy stored in the elastic polymers. Let us first derive a balance equation for this elastic energy. In an elastic spring model, where the connector force \mathbf{F} in general is $\mathbf{F} = \mathbf{F}(\mathbf{Q})$

[†] Sometimes the pressure strain is written as $\Pi_{\alpha\alpha} = -\overline{u'_\alpha \partial p' / \partial x_\alpha} = \overline{p' \partial u'_\alpha / \partial x_\alpha} - \overline{u'_\alpha p'}$, which is the sum of the pressure strain and pressure transport in our case. However, we use the definition of (5.16), as in this case $\sum_\alpha \Pi_{\alpha\alpha} = 0$.

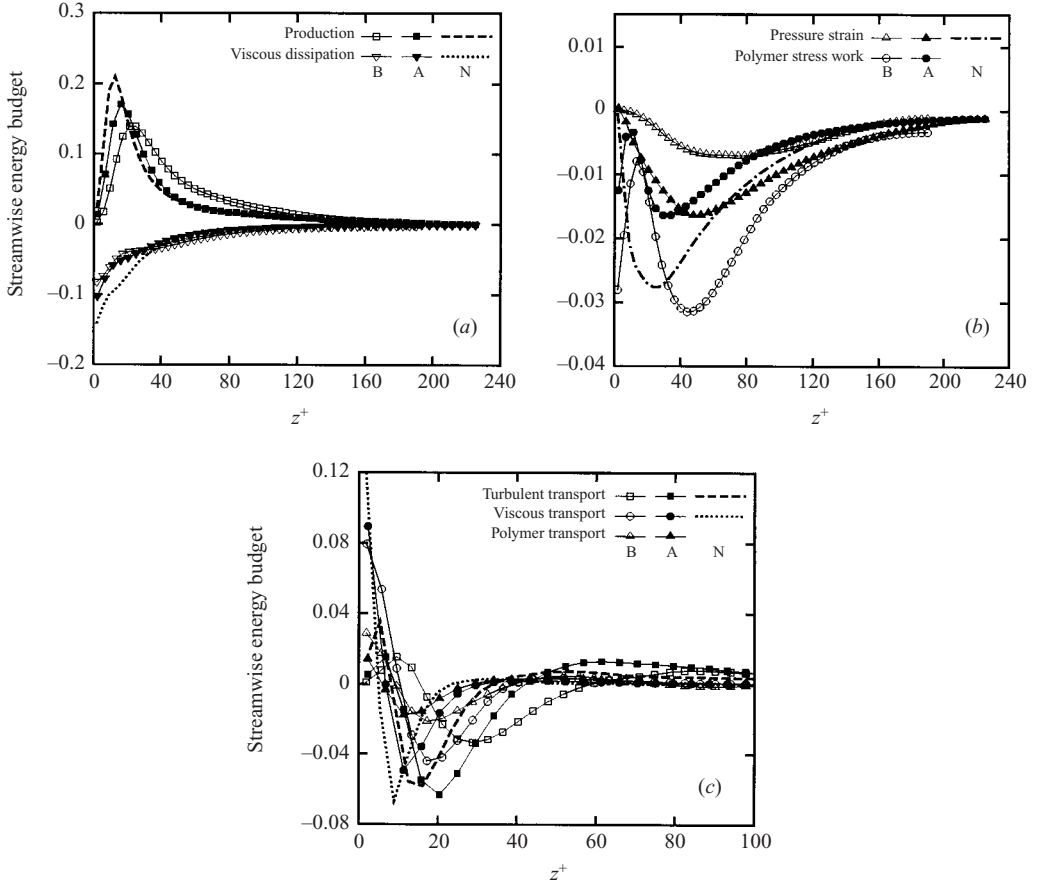


FIGURE 12. The turbulent kinetic energy budgets of the streamwise direction ($\frac{1}{2}\overline{u'^2}$) as a function of the distance from the wall z^+ for Newtonian flow (thick lines) and for the FENE-P model with $\beta = 0.6$, $We_* = 54$ and $b = 100$ (run A, closed symbols) and $b = 1000$ (run B, open symbols). (a) production (P_{xx}) and viscous dissipation ($-\epsilon_{xx}$); (b) pressure strain (Π_{xx}) and polymer stress work ($-W_{xx}$); (c) transport by turbulent stress ($T_{xx}^{(r)}$), viscous (solvent) stress ($T_{xx}^{(s)}$) and polymer stress ($T_{xx}^{(p)}$). The transport by pressure fluctuations ($T_{xx}^{(\pi)}$) is negligibly small and is not shown here. Only $z^+ < 100$ is shown as all transport terms are almost zero in the centre of the channel.

with \mathbf{Q} the extension of the spring, the elastic energy P is equal to

$$P = \int \mathbf{F}(\mathbf{Q}) d\mathbf{Q}. \tag{5.17}$$

This has to be multiplied by n (the number of polymers per unit volume) to obtain the elastic energy per unit volume. For the FENE-P model where the force $\mathbf{F}^{(c)}$ is specified by (2.6), the polymer energy becomes

$$P = n \int \mathbf{F}(\mathbf{Q}) d\mathbf{Q} = -\frac{nH Q_0^2}{2} \ln \left(1 - \frac{\langle Q^2 \rangle}{Q_0^2} \right) = \frac{1}{2} n k T b \ln f, \tag{5.18}$$

with $f = f(\text{trc})$ specified in (2.9). Taking the trace of the equations for the polymer stress (2.7) and the evolution of the polymer conformation tensor (2.8) we find (in

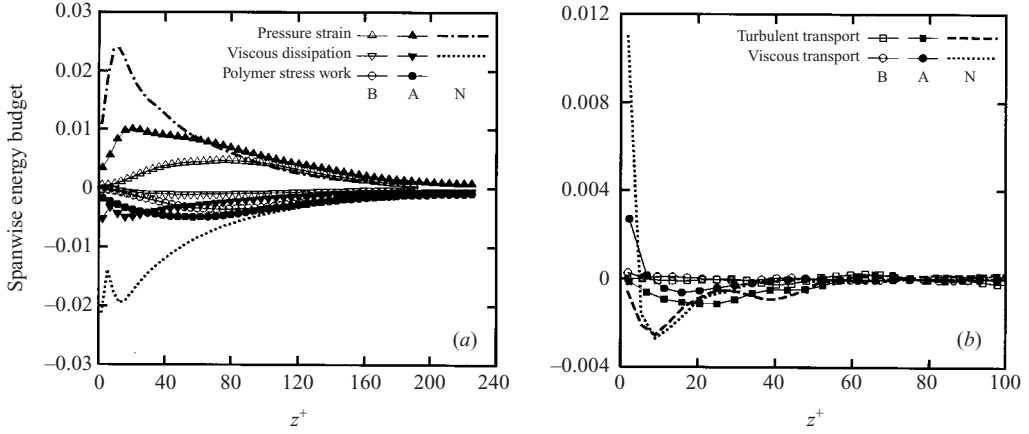


FIGURE 13. The turbulent kinetic energy budgets of the spanwise direction ($\frac{1}{2}\overline{v'^2}$) as a function of the distance from the wall z^+ for Newtonian flow (thick lines) and for the FENE-P model with $\beta = 0.6$, $We_* = 54$ and $b = 100$ (run A, closed symbols) and $b = 1000$ (run B, open symbols). (a) pressure strain (Π_{vv}), viscous dissipation ($-\epsilon_{vv}$) and polymer stress work ($-W_{vv}$); (b) transport by turbulent stress ($T_{vv}^{(r)}$) and viscous (solvent) stress ($T_{vv}^{(s)}$). The transport by pressure fluctuations ($T_{vv}^{(\pi)}$) and polymer stress ($T_{vv}^{(p)}$) is negligibly small and is not shown here. Only $z^+ < 100$ is shown as all transport terms are almost zero in the centre of the channel.

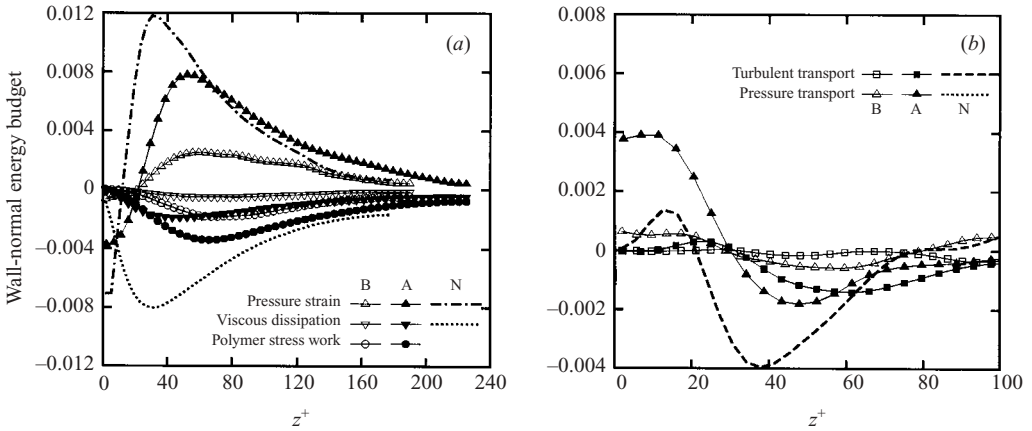


FIGURE 14. The turbulent kinetic energy budgets of the wall-normal direction ($\frac{1}{2}\overline{w'^2}$) as a function of the distance from the wall z^+ for Newtonian flow (thick lines) and for the FENE-P model with $\beta = 0.6$, $We_* = 54$ and $b = 100$ (run A, closed symbols) and $b = 1000$ (run B, open symbols). (a) pressure strain (Π_{ww}), viscous dissipation ($-\epsilon_{ww}$) and polymer stress work ($-W_{ww}$); (b) transport by turbulent stress ($T_{ww}^{(r)}$) and pressure fluctuations ($T_{ww}^{(\pi)}$). The transport by viscous (solvent) stress ($T_{ww}^{(s)}$) and polymer stress ($T_{ww}^{(p)}$) is negligibly small and is not shown here. Only $z^+ < 100$ is shown as all transport terms are almost zero in the centre of the channel.

index notation)

$$\tau_{ii}^{(p)} = nkT(-3 + fc_{ii}) \quad (5.19)$$

and

$$\frac{Dc_{ii}}{Dt} = \frac{\partial c_{ii}}{\partial t} + u_j \frac{\partial c_{ii}}{\partial x_j} = 2 \frac{\partial u_i}{\partial x_j} c_{ij} + \frac{1}{\lambda}(3 - fc_{ii}). \quad (5.20)$$

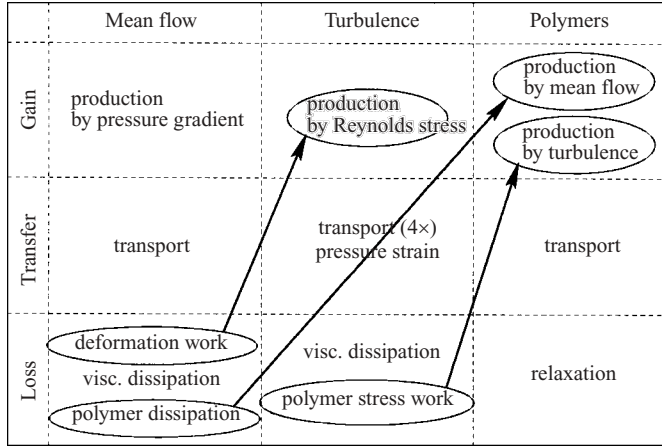


FIGURE 15. The various terms of the energy budgets for mean flow kinetic energy, turbulent fluctuations kinetic energy, elastic energy and their interactions.

The time derivative of the polymer energy follows from (5.18):

$$\frac{\partial P}{\partial t} = \frac{1}{2}nkTb \frac{1}{f} \frac{\partial f}{\partial c_{ii}} \frac{\partial c_{ii}}{\partial t} = \frac{1}{2}nkTf \frac{\partial c_{ii}}{\partial t}, \tag{5.21}$$

and a similar expression can be obtained for $\partial P/\partial x_j$. Combining (2.7), (5.19), (5.20) and (5.21) gives for the material derivative of the polymeric elastic energy

$$\frac{DP}{Dt} = \frac{\partial P}{\partial t} + u_j \frac{\partial P}{\partial x_j} = \tau_{ij} \frac{\partial u_i}{\partial x_j} - \frac{1}{2\lambda} f \tau_{ii}^{(p)}. \tag{5.22}$$

Applying the Reynolds decomposition to the polymer energy ($P = \bar{P} + P'$) to this equation leads to

$$\begin{aligned} \frac{D\bar{P}}{Dt} &= \frac{\partial \bar{P}}{\partial t} + U_j \frac{\partial \bar{P}}{\partial x_j} \\ &= -\frac{\partial}{\partial x_j} \overline{(u'_j P')} + \bar{\tau}_{ij}^{(p)} \frac{\partial U_i}{\partial x_j} + \overline{\tau'_{ij}{}^{(p)}} \frac{\partial u'_i}{\partial x_j} - \frac{1}{2\lambda} \overline{f \tau_{ii}^{(p)}}. \end{aligned} \tag{5.23}$$

The first term on the second line denotes the transport of elastic energy by velocity fluctuations, the next two terms denote the interaction of the polymers with the mean and fluctuating velocity field, respectively, and the last term can be recognized as a dissipative term. We see that the two interaction terms are exactly equal to the polymeric dissipation of mean flow kinetic energy W_u in (5.1) and the polymer stress work W_{ii} in (5.7). The dissipative term is the transfer of energy from polymers into heat by relaxation of the polymers from an extended state to their equilibrium state. Note that in this term the relaxation time appears as a timescale in which elastic energy is dissipated.

The interaction between the various processes in the budgets of the kinetic and elastic energy is schematically illustrated in figure 15.

In figure 16 we have plotted the various contributions to the elastic energy budget (except the transport term, which is negligibly small) for two different polymer simulations. From this figure it follows that close to the wall the balance reduces to a difference between two large terms, i.e. mean flow production and dissipative

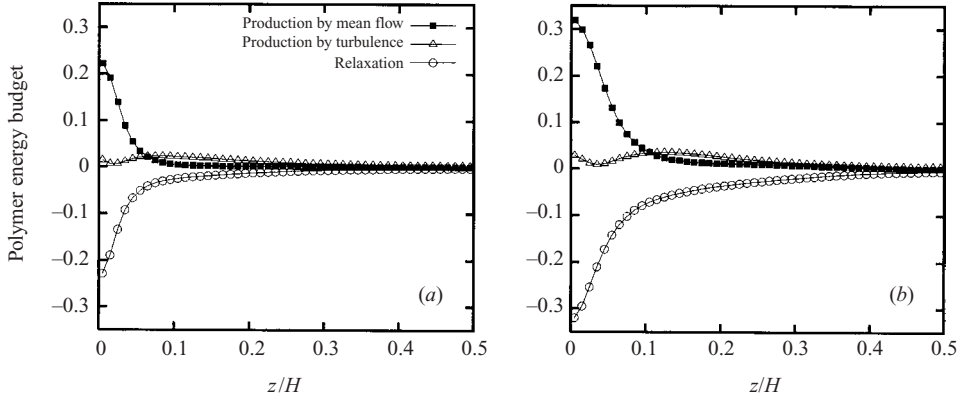


FIGURE 16. Polymer energy budgets (see (5.23)) as a function of the distance from the wall z/H for the FENE-P model. (a) run A ($\beta=0.6$, $We_* = 54$ and $b=100$); (b) run B ($\beta=0.6$, $We_* = 54$ and $b=1000$). The transport term is negligible and is therefore not shown here.

relaxation. Further away from the wall, i.e. in the the buffer layer, the production by the fluctuating velocity field becomes larger than the mean flow term. However, the largest contribution in total comes from the mean flow which is consistent with the importance of the polymer stresses in the mean momentum balance at large drag reduction.

6. Pressure fluctuations

Pressure fluctuations in turbulent flows play an important role in turbulence modelling. For a review on the role of pressure in turbulence we refer to Willmarth (1975) and Eckelmann (1988). As we discussed in the previous section, an important effect of the polymers was found to be the reduction of the pressure strain in the turbulent kinetic energy budget. Therefore we will now investigate pressure fluctuations in our simulations and their role in the energy budget more in detail. In figure 17 we show the root mean square of the pressure fluctuations as a function of distance from the wall. We note that our results for the Newtonian case are in good agreement with the results of Kim (1989). This figure shows that the pressure fluctuations are damped for viscoelastic flow over the entire channel height. The effect is stronger as drag reduction increases. Also we observe that the maximum of the r.m.s. is located further away from the wall, which again indicates the thickening of the buffer region.

To study the pressure in detail we write the Poisson equation for the pressure (which is the divergence of the fluctuating part of (3.1)) in the following way:

$$\frac{\partial^2 p'}{\partial x_i^2} = \frac{\partial^2}{\partial x_i \partial x_j} (-u'_i U_j - U_i u'_j) + \frac{\partial^2}{\partial x_i \partial x_j} (-u'_i u'_j + \overline{u'_i u'_j}) + \frac{\partial^2}{\partial x_i \partial x_j} \tau'_{ij}{}^{(p)}. \quad (6.1)$$

From the right-hand side of this equation it can be seen that the pressure fluctuations consist of three parts. Therefore we can decompose the pressure fluctuation into these three contributions, by writing $p' = p'_{rapid} + p'_{slow} + p'_{polymer}$, which stand for the 'rapid', 'slow' and 'polymer' pressure, and these are defined by

$$\frac{\partial^2 p'_{rapid}}{\partial x_i^2} = \frac{\partial^2}{\partial x_i \partial x_j} (-u'_i U_j - U_i u'_j), \quad (6.2)$$

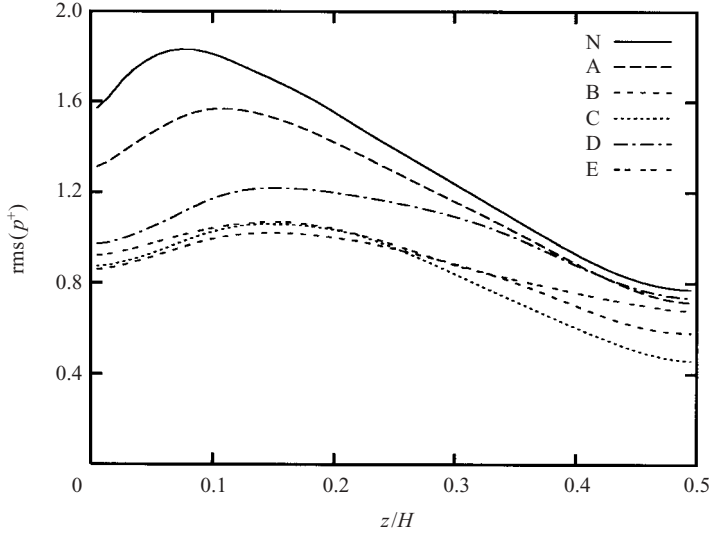


FIGURE 17. Root mean square of the pressure fluctuations as a function of the distance from the wall z/H for Newtonian flow and for all the simulations with the FENE-P model.

$$\frac{\partial^2 p'_{slow}}{\partial x_i^2} = \frac{\partial^2}{\partial x_i \partial x_j} (-u'_i u'_j + \overline{u'_i u'_j}), \quad (6.3)$$

$$\frac{\partial^2 p'_{polymer}}{\partial x_i^2} = \frac{\partial^2}{\partial x_i \partial x_j} \tau'_{ij}(p). \quad (6.4)$$

The background to the splitting of the pressure is given by Wilcox (1993) and Kim (1989). In short, we can say that the rapid part is due to the deformation by the mean flow field and the nonlinear slow part is caused by the interaction of turbulence. The polymer part depends on the fluctuating polymer stress. Now, by solving these three Poisson equations we can compute the individual pressure contributions.

In figure 18 we show the r.m.s. of the pressure fluctuation subdivided into the three contributions discussed above. The results for the Newtonian case are shown together with two viscoelastic simulations. We see that the rapid part is reduced near the wall, but it is slightly increased in the centre of the channel (in particular for case B). As this contribution is due to the mean flow, this effect is the direct result of the change in the mean velocity profile. The slow part, that accounts for the nonlinear turbulence effects, is smaller than the Newtonian results almost everywhere and this effect becomes stronger with increasing drag reduction. Furthermore we find that for the Newtonian flow the slow part is larger than the rapid part almost everywhere in the channel, while for case B they become of the same order of magnitude. As we have seen that drag reduction generally leads to damping of turbulence (e.g. the Reynolds stress reduction shown figure 7), this manifests itself in this case primarily as reduction of the nonlinear (slow) part. The influence of the polymers results in an increase of pressure fluctuations with increasing drag reduction, which is opposite to the general reduction of the other pressure contributions. For case B the polymer contribution is about 20% of the total pressure fluctuations.

The individual contributions by the three pressure fluctuations to the pressure-strain term in the streamwise direction Π_{xx} are shown in figure 19. We saw in figure 12(b) that the total pressure strain is strongly reduced with increasing drag reduction and

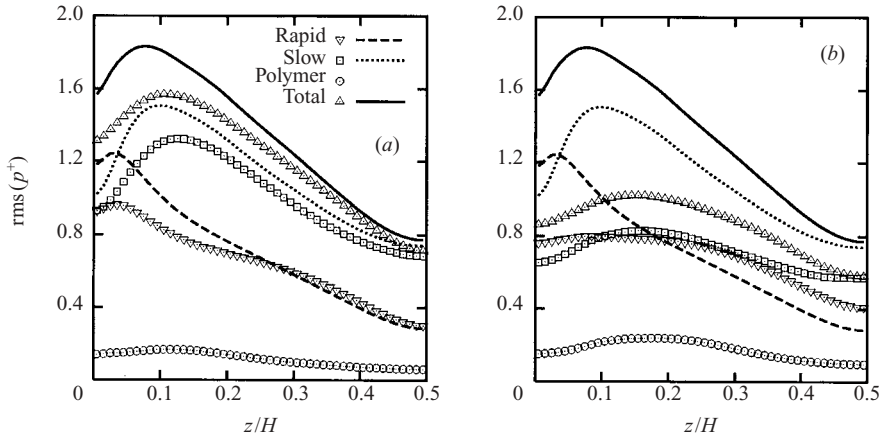


FIGURE 18. Root mean square of the rapid, slow and polymer pressure contributions as a function of the distance from the wall z/H . (a) Comparison of Newtonian flow (lines) and the FENE-P model with $\beta = 0.6$, $We_* = 54$ and $b = 100$ (case A, symbols). (b) Comparison of Newtonian flow (lines) and the FENE-P model with $\beta = 0.6$, $We_* = 54$ and $b = 1000$ (case B, symbols).

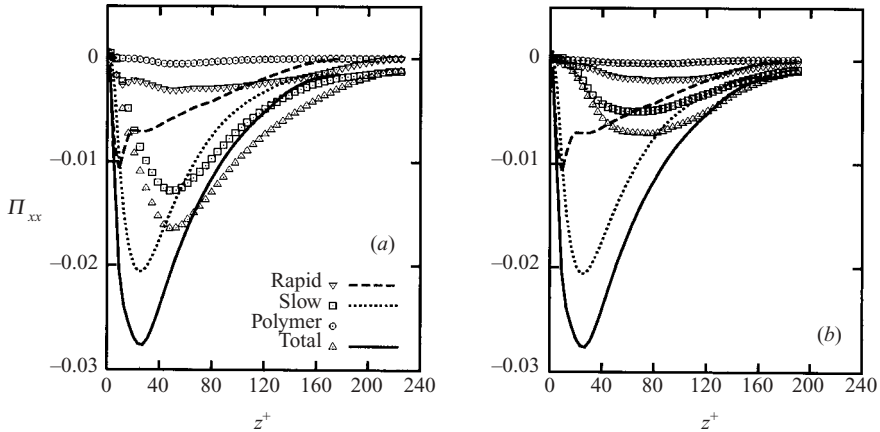


FIGURE 19. The contributions to the streamwise pressure strain by the three pressure fluctuations as a function of the distance from the wall z^+ . (a) Comparison of Newtonian flow (lines) and the FENE-P model with $\beta = 0.6$, $We_* = 54$ and $b = 100$ (case A, symbols). (b) Comparison of Newtonian flow (lines) and the FENE-P model with $\beta = 0.6$, $We_* = 54$ and $b = 1000$ (case B, symbols).

the maximum values becomes located further away from the wall. Regarding the three individual contributions, we see that each of these contributions is also reduced but their relative magnitude stays about the same. The polymer part of the total pressure strain is negligible and this means that polymer stresses do not contribute to the exchange of kinetic energy among the three velocity components.

7. Shear sheltering in turbulent drag reduction

In this section we present some ideas on a mechanism for turbulent drag reduction by polymers. To this end we present and discuss covariance data in the buffer layer in

Newtonian and polymer flows. Let us first consider a shear-free turbulent boundary layer over a surface (i.e. the mean velocity and the dissipation do not vary with the height). The wall-normal velocities of a large turbulent eddy (centred at a height z_1 above the surface, velocity w_l) and a small eddy (centred at a height z , velocity w_s) are only very weakly correlated, thus $\overline{w_l w_s} \simeq 0$ (Hunt *et al.* 1989). The velocity at height z above the surface will, however, be slightly modified by the induced velocity of the large eddy given by

$$w(z) \simeq w_s + \frac{z}{z_1} w_l. \quad (7.1)$$

Multiplying this result by the velocity of the large eddy $w_l \equiv w(z_1)$ and ensemble averaging gives the following cross-covariance of the velocities at heights z and z_1 :

$$\overline{w(z)w(z_1)} \simeq \frac{z}{z_1} \overline{w(z_1)w(z_1)}. \quad (7.2)$$

Thence the ‘top-down’ normalized covariance has the form

$$\hat{R}_{ww}(z, z_1) = \frac{\overline{w(z)w(z_1)}}{w^2(z_1)} \simeq \frac{z}{z_1} \quad \text{for } z < z_1. \quad (7.3)$$

In turbulent layers with shear this covariance can be generalized according to Hunt *et al.* (1989) and becomes

$$\hat{R}_{ww}(z, z_1) \simeq f\left(\frac{z}{z_1}\right) \quad \text{for } z < z_1. \quad (7.4)$$

This self-similar form has been measured in many types of complex boundary layers (Hunt *et al.* 1989 and references therein). Here, z_1 varies over the channel height and the data collapse on a single curve. For $Re \rightarrow \infty$ the effect of shear is less, so that relation (7.4) approaches (7.3). In figure 20(a) this covariance is shown for our direct numerical simulations of Newtonian flow. It is very clear that the data collapse on a single curve for an extensive range of z_1 , proving the self-similarity of (7.4). The correlation R_{ww} , usually defined normalized in the conventional way, i.e. with

$$\sqrt{\overline{w^2(z)} \overline{w^2(z_1)}},$$

is not self-similar.

In figures 20(b) and 20(c) we present $\hat{R}_{ww}(z, z_1)$ for two viscoelastic simulations (cases A and B). We see that for a small extensibility parameter (case A, figure 20b), the self-similar behaviour is still present and the normalized covariance for the viscoelastic case does not differ from the Newtonian. However, as the extensibility parameter and drag reduction increase, figure 20(c), a significant decrease of this correlation is observed except for the smallest value of z_1 . Also, the self-similar form of the curves is no longer found.

Our explanation for this behaviour begins with a consideration of how large eddies in a turbulent flow approach a rigid boundary. If there is no mean shear the wall-normal velocity component of these eddies is damped and its integral length scale is also greatly reduced. In the presence of strong shear in the buffer layer near the wall, the length scale is further reduced. Thus, although the shear production of small-scale eddies, that dominates the turbulence process in the wall layer, increases, there is a blocking or ‘shear sheltering’ (Hunt & Durbin 1999) mechanism at some distance from the wall. As a consequence of this damping of the larger-scale eddies, they are blocked and are prevented from penetrating into the near-wall region. The interactions

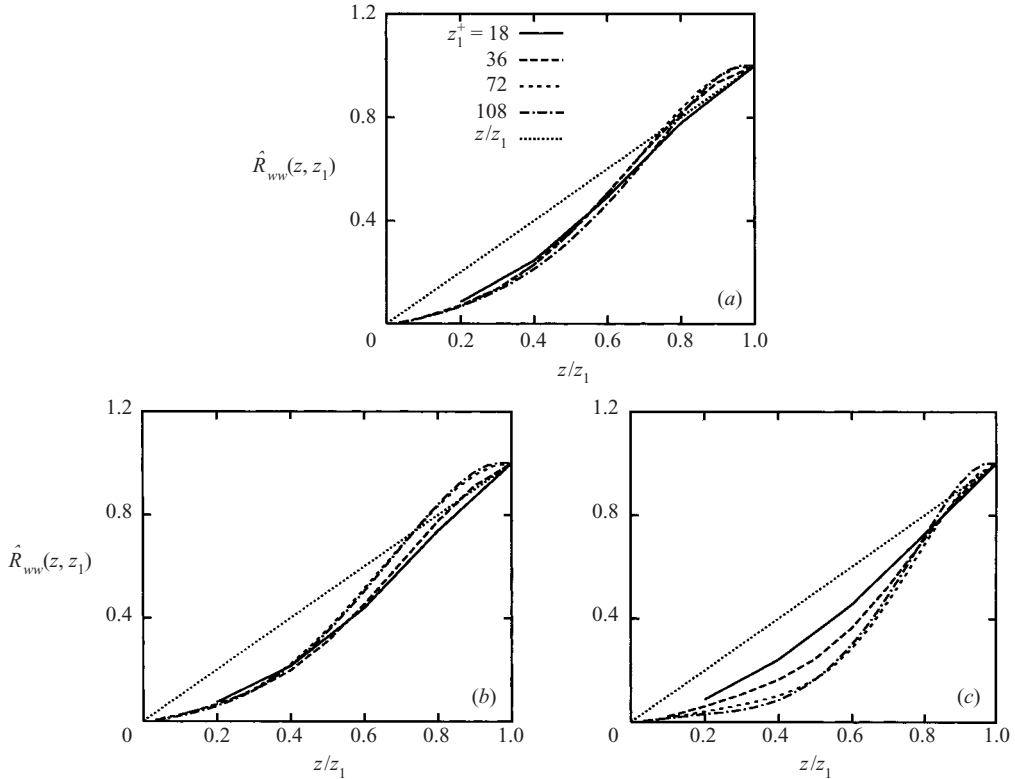


FIGURE 20. The cross-correlation of the wall-normal velocities (see (7.3)) computed by DNS. (a) Newtonian flow (case N); (b) FENE-P model with $\beta = 0.6$, $We_* = 54$ and $b = 100$ (case A); (c) FENE-P model with $\beta = 0.6$, $We_* = 54$ and $b = 1000$ (case B).

between the structures below and above the layer are significantly reduced, especially in a Newtonian flow at low and moderate Reynolds numbers. Indeed some models of near-wall dynamics effectively ignore interactions with the outer flow. This is not consistent with most data and experiments, especially at very high Reynolds numbers (Hunt & Morrison 2000).

Our hypothesis is that the addition of polymers means in physical terms a strengthening of the shear sheltering mechanism. A sketch of the process is shown in figure 21. At the top of the buffer layer, since here the rate of straining is maximum in a Newtonian flow, the polymer stretching rate is large and damps the wall-normal fluctuations (Lumley 1969). This leads to blocking of the large eddies coming from the centre of the channel. These have a velocity \mathcal{U} and a length scale \mathcal{L} and cause amplification of streamwise velocity fluctuations over the lifetime \mathcal{L}/\mathcal{U} of the eddies at the top of the buffer layer. But the natural Kelvin–Helmholtz instability of this shear layer is also suppressed by the action of the polymers, so that there is an increase in the time taken for the breakdown of this local shear layer as seen by the signal of the wall-normal velocity (normalized similarly to the covariance \hat{R}_{ww}) in figure 22. A similar shear sheltering effect is seen when damped wall-normal free-stream turbulence drives instabilities at the top of a laminar boundary layer (Wu *et al.* 1999). Furthermore, both the intense shear and the stability of the layer reduce the wall-normal velocity fluctuations below this layer. This is in agreement with our

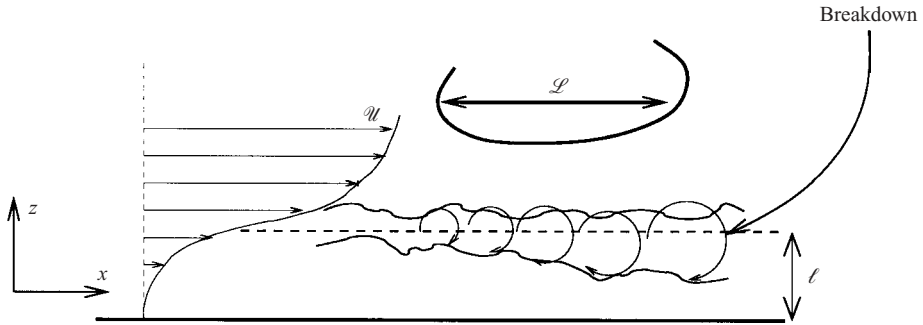


FIGURE 21. Simplified sketch of the shear sheltering mechanism. The maximum of the velocity gradient is located at the top of the shear sheltering layer, where in connection with the large velocity gradient disturbances are growing by the Kelvin–Helmholtz mechanism and finally break down. The momentum transport resulting from these disturbances is then transmitted through the shear sheltering layer by viscous effects. Indicated are a velocity scale u (the bulk velocity of the friction velocity), a macroscopic length scale L (e.g. the size of large eddies or a length scale depending on the channel dimensions) and a microscopic length scale l (the thickness of the shear sheltering layer).

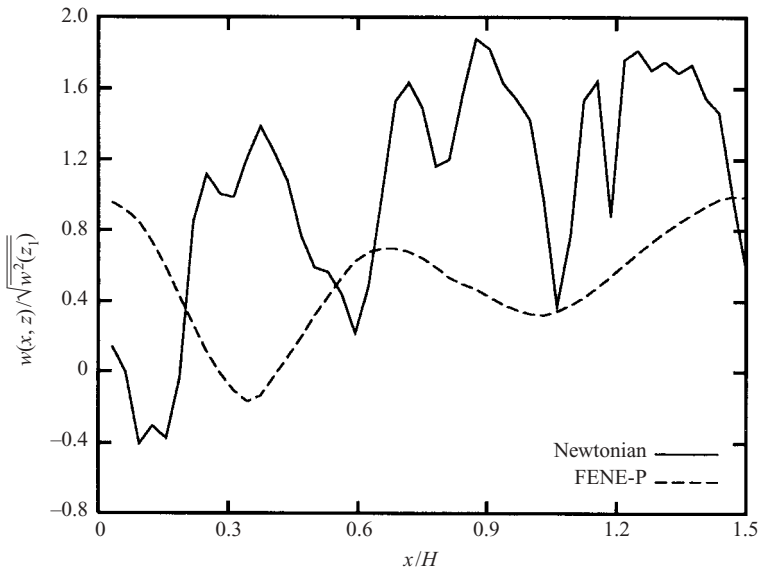


FIGURE 22. The wall-normal velocity $w(x, z)$ along the streamwise direction normalized like the covariance in equation (7.3) for Newtonian flow and for run B. $z_1^+ = 20$, $z_1^+ = 60$.

computed flow statistics which indicate that most turbulent activity is moved away from the wall and that the finite thickness of the buffer layer increases. However, this layer does not fill the entire flow as proposed by some authors.

Although there is a strong decrease of the mean level of interactions of the flow in the regions above and below the shear sheltering layer, the upper region nevertheless affects that below, where the wall shear stress is generated. It is likely that the intermittent breakdown of the layer provides the mechanism for the interaction with the outer flow and the determination of the wall shear stress. This is the basis for our order-of-magnitude model. The nonlinear wavelike fluctuation of the buffer layer

with polymers shown in figure 22 is consistent with de Gennes (1990) ‘elastic’ concept. This is also supported by the data of McComb & Rabie (1979, 1982), Sreenivasan & White (2000) and Min *et al.* (2003).

First we balance the inertial and viscous terms in this shear layer. The inertial terms can be estimated as $\mathcal{U}^2/\mathcal{L}$, the viscous terms as $\nu\mathcal{U}/\ell^2$, where \mathcal{U} is a characteristic macroscopic velocity scale, whose order of magnitude lies between the mean velocity U_b and the friction velocity u_* . The macroscopic length scale \mathcal{L} is of the order of the channel height and the microscopic length scale ℓ is of the order of the thickness of the shear sheltering layer. The dynamics of the shear sheltering layer with strong polymer actions is quite different from that of the wall layer in a Newtonian flow, because its considerable stability means that the time scale is determined by the outer flow. Therefore

$$\frac{\mathcal{U}^2}{\mathcal{L}} \sim \frac{\nu\mathcal{U}}{\ell^2} \quad (7.5)$$

so that the ratio of ℓ to \mathcal{L} is given by

$$\frac{\ell}{\mathcal{L}} \sim \left(\frac{\nu}{\mathcal{U}\mathcal{L}} \right)^{1/2} = Re^{-1/2} \quad \text{if } \mathcal{U} \sim U_b \quad (7.6)$$

and by

$$\frac{\ell}{\mathcal{L}} \sim \left(\frac{\nu}{\mathcal{U}\mathcal{L}} \right)^{1/2} = Re^{-1/2} \left(\frac{U_b}{u_*} \right)^{1/2} = Re^{-1/2} C_F^{-1/4} \quad \text{if } \mathcal{U} \sim u_*. \quad (7.7)$$

This shows why with polymers the wall layer thickness ℓ is much greater than in a Newtonian flow where

$$\frac{\ell}{\mathcal{L}} \sim Re^{-1} C_F^{-1/2}. \quad (7.8)$$

Since the wall stress τ in this model is of the order $\tau \sim \rho\nu\mathcal{U}/\ell$, depending on the estimate of \mathcal{U} , the friction coefficient C_F (4.2) can now be derived as

$$C_F \sim Re^{-1/2} \quad \text{for } \mathcal{U} \sim U_b, \quad (7.9)$$

$$C_F \sim Re^{-2/3} \quad \text{for } \mathcal{U} \sim u_*. \quad (7.10)$$

These results can be compared with the maximum drag reduction asymptote (4.5), which can be approximated by a power-law expression of the form $C_F = ARe^{-n}$ with $n \simeq 0.55$ (Virk *et al.* 1967) or $n \simeq 0.58$ (Virk 1975) and which is valid for middle-range Reynolds numbers $4000 < Re < 40000$. Our estimate based on the shear sheltering effect is broadly consistent with the power law for the Virk asymptote.

Note that for $\mathcal{U} \sim u_*$ a macroscopic time scale of the flow can be defined by $\tau_f = \mathcal{L}/u_*$. A comparison of this time scale with the relaxation time of the polymer λ gives

$$\frac{\lambda}{\tau_f} \sim \frac{\lambda u_*}{\mathcal{L}}, \quad (7.11)$$

which is a Weissenberg number based on macroscopic variables. Typically the macroscopic length scale $\mathcal{L} \sim 0.1H$, which gives for this Weissenberg number $We > 1$. Thus the proposed mechanism is consistent with the polymer physics.

8. Conclusion and discussion

We have performed direct numerical simulations for a turbulent flow of a Newtonian fluid with dissolved polymers. The polymers are modelled by means of a realistic

constitutive equation, the FENE-P model. The coupling between the polymers and the flow field is two-way, i.e. the polymers are deformed by the velocity field and the resulting polymer stress is returned into the momentum equations of the flow. The flow is fully turbulent all the time. In the polymer model we have varied three parameters: the extensibility parameter b , which is proportional to the square of the maximum polymer length, the ratio β of the solvent to the total zero-shear-rate viscosity, which determines the polymer concentration and the Weissenberg number We_* , which is the ratio of the relaxation time λ of the polymers to the turbulence time scale. Necessary criteria to obtain the maximum drag reduction asymptote are, besides a sufficiently high Reynolds number, highly extensible polymers and a high polymer concentration. We have selected flow conditions and polymer characteristics such that our simulations are very close to the maximum drag reduction or Virk (1975) asymptote.

As the pressure drop is kept constant in our simulations drag reduction is manifested as an increase of the mean or bulk velocity. With respect to the mean velocity profile we find both in experiment and our simulations only an offset in the additive constant of the logarithmic profile for the Newtonian flow. At high drag reduction we find also a large increase of the slope of the profile. Especially in the latter cases the buffer layer is significantly thickened, as the logarithmic profile starts further away from the wall. No changes are found in the viscous sublayer. The changes of the mean velocity profile are qualitatively and quantitatively in excellent agreement with the experiments of den Toonder *et al.* (1997) and Ptasinski *et al.* (2001).

The peak value of the r.m.s of the streamwise velocity fluctuations increases with increasing parameter b compared to Newtonian flow. At the same time the maximum of the r.m.s. of the streamwise velocity is located further away from the wall, reconfirming the thickened buffer layer. For the simulation of the highest drag reduction case, which also has the largest Weissenberg number, we find that the peak value is reduced again. Such behaviour, i.e. increasing and then decreasing peak values of the streamwise velocity fluctuations when drag reduction increases to its maximum value, have also been found in the experiments. A difference between our simulation and the experiments is that the changes in the simulations are larger than in the experiments. This might be related to shortcomings of the FENE-P model. Especially in time-dependent elongational flows (see Herrchen & Öttinger 1997; Keunings 1997) the FENE-P model fails to fully represent the rheological behaviour. A possible solution would be to perform Brownian dynamics simulations, e.g. by using the Brownian configuration fields method (Hulsen, Van Heel & Van den Brule 1997). This method makes it possible to use the FENE model (without the Peterlin approximation), but as it does not provide a single closed-form constitutive equation, the computational requirements are much more demanding.

The r.m.s. of the spanwise and wall-normal velocity fluctuations show a decrease and a shift away from the wall monotonically with increasing drag reduction. This agrees very well with the experiments. The Reynolds stress is strongly decreased, though less than in the experiments. The resulting Reynolds stress deficit is compensated by a polymer shear stress which for the highest drag-reduction cases is 40%–50% of the total stress. Contrary to observations of Warholic *et al.* (1999a) but in agreement with those of Ptasinski *et al.* (2001) the Reynolds stress does not vanish at maximum drag reduction. Computational results for the polymer length show a high extension of the polymers compared to their length in equilibrium, especially in the neighbourhood of the wall. It follows that the ability of polymers to stretch is an essential ingredient for high polymer drag reduction.

The analysis of the kinetic energy budgets shows that the pressure-strain term, which is responsible for energy transfer from the streamwise direction to the other directions, is the most reduced term in the budget and this explains the enhanced anisotropy of the flow. Furthermore, the polymer stress work is found to be positive for all cases, which means that polymers dissipate (and not produce) energy. The highest dissipation by polymers is in the buffer layer, in contrast to the viscous dissipation which is maximal at the wall. The polymer dissipation of the mean flow and the turbulent kinetic energy are transferred into elastic energy of the polymers which in its turn is then dissipated by polymer relaxation.

Finally, from an analysis of cross-correlations we conclude that drag reduction produces a strong shear sheltering layer near the wall in the buffer layer. The result is a decoupling of the structures above and below this layer. From an analysis of various length scales we find a power-law behaviour for the friction coefficient as a function of the Reynolds number, which resembles the behaviour of the maximum drag reduction asymptote. So the changes of the flow statistics and structures in the buffer layer in combination with the shear sheltering mechanism play a key role in the high drag reduction regime.

Discussions with Professor A. N. Beris and Dr. R. Sureshkumar are gratefully acknowledged.

Appendix. Effect of variation of the artificial diffusion constant

In § 3 and more precisely in the integration procedure for the polymer conformation tensor, (3.3), we introduced an artificial diffusivity term $\kappa/(u_*H) \nabla^2 \mathbf{c}$, which has to be added to (3.2) for numerical reasons to avoid instabilities. However, this term should not have too much influence on the macroscopic flow parameters like velocities and stresses. A detailed study on the effect of the artificial stress diffusivity on the stability of viscoelastic flow calculations is given by Sureshkumar & Beris (1995). In this Appendix we will briefly summarize the reason of the introduction of this term and its effect on the system of equations and we will show for selected results that the artificial diffusivity does not significantly alter the result.

Viscoelastic calculations not only introduce extra variables like the polymer conformation and stress, but more importantly they can lead to a change in the type of the total system of equations for the momentum and for the polymer conformation tensor (Joseph 1990). This is in particular the case for high Weissenberg number problems. A detailed analysis of the type of equations and its consequences for numerical methods is provided by Keunings (1989). The change of type is associated with the loss of evolution, which leads to an instability in which short waves will grow in amplitude (Dupret & Marchal 1986; Joseph & Saut 1986; Marchal & Crochet 1987). In our problem this will lead to a violation of the positive definiteness of the polymer conformation tensor \mathbf{c} , which is an essential property of this tensor. In principle, for most differential models the conformation tensor will remain positive definite as long as it is positive definite initially (Hulsen 1990). However, in a computation this property can be lost due to numerical errors during time integration.

Positive definiteness and thus stability can be conserved by using so-called ‘streamwise upwinding’, as is often done in finite element techniques (e.g. Marchal & Crochet 1987). In our case this will lead to less accuracy. Min, Yoo & Choi (2001) and Dubief & Lele (2001) have used an algorithm consisting of a Crank–Nicolson method and a third-order Runge–Kutta method, which increases stability.

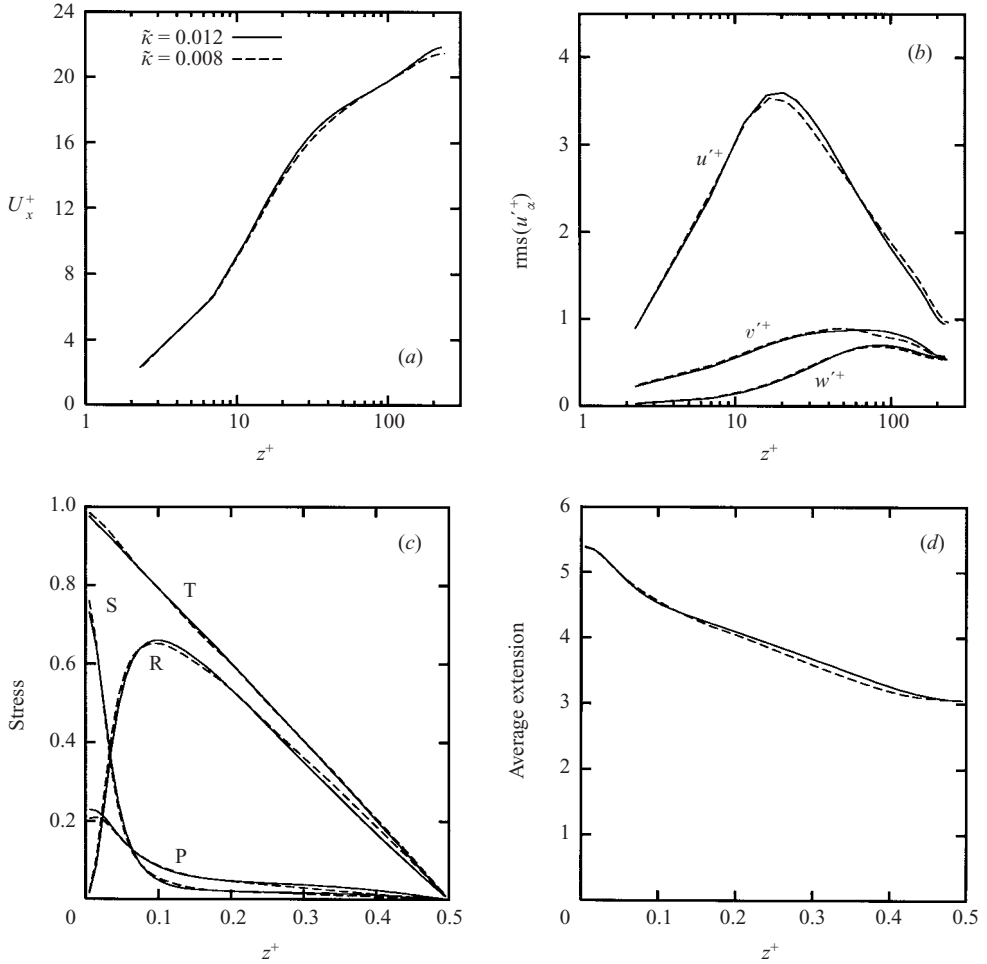


FIGURE 23. (a) Mean streamwise velocity profile as function of the distance from the wall z^+ with the FENE-P model (parameters $\beta = 0.6$, $We_* = 54$ and $b = 100$) for two different values of the artificial diffusivity $\tilde{\kappa}$. (b) As (a) but for root mean square profiles of the velocity fluctuations u'^+ : streamwise component; v'^+ : spanwise component; w'^+ : wall-normal component (c). As (a) but for various shear stress contributions. R: Reynolds stress; S: solvent (viscous) stress; P: polymer stress; T: total stress. (d) As (a) but for mean polymer extension.

Another possibility is the use of so-called ‘streamline diffusivity’ which is proposed by Sureshkumar & Beris (1995) and which is also applied in this paper. As we stated before, this will increase stability, but should not alter the main results significantly. To show this, we compare the results of one of our viscoelastic turbulent simulations (run A, with $\beta = 0.6$, $We_* = 54$ and $b = 100$ and $\tilde{\kappa} = \kappa/(u_*H) = 0.012$) with a simulation with the same parameters in the FENE-P model but with $\kappa/(u_*H) = 0.008$. This comparison is shown for some selected statistics in figure 23. These figures clearly show that the difference is very small, providing us with evidence that the addition of a small amount of artificial diffusivity does not significantly modify the simulation results.

REFERENCES

- BIRD, R. B., CURTISS, C. F., ARMSTRONG, R. C. & HASSAGER, O. 1987 *Dynamics of Polymer Liquids*, 2nd edn, vol. 2. John Wiley.
- BIRD, R. B., DOTSON, P. J. & JOHNSON, N. L. 1980 Polymer solution rheology based on a finitely extensible bead-spring chain model. *J. Polymer Sci. Polymer Lett.* **7**, 213–235.
- BONN, D., COUDER, Y., VAN DAM, P. H. J. & DOUADY, S. 1993 From small scales to large scales in three-dimensional turbulence: the effect of diluted polymers. *Phys. Rev. E* **47**, R28–R31.
- CADOT, O., DOUADY, S. & COUDER, Y. 1995 Characterization of the low-pressure filaments in a three-dimensional turbulent shear flow. *Phys. Fluids* **7**, 630–646.
- DEAN, R. B. 1978 Reynolds number dependence of skin friction and other bulk flow variables in two-dimensional rectangular duct flow. *Trans. ASME: J. Fluids Engng* **100**, 215–223.
- DIMITROPOULOS, C. D., SURESHKUMAR, R. & BERIS, A. N. 1998 Direct numerical simulation of viscoelastic turbulent channel flow exhibiting drag reduction: effect of the variation of rheological parameters. *J. Non-Newtonian Fluid Mech.* **79**, 433–468.
- DOUADY, S., COUDER, Y. & BRACHET, M. E. 1991 Direct observation of the intermittency of intense vorticity filaments in turbulence. *Phys. Rev. Lett.* **67**, 983–986.
- DRAAD, A. A., KUIKEN, G. D. C. & NIEUWSTADT, F. T. M. 1998 Laminar-turbulent transition in pipe flow for Newtonian and non-Newtonian fluids. *J. Fluid Mech.* **377**, 267–312.
- DUBIEF, Y. & LELE, S. K. 2001 Direct numerical simulation of polymer flow. *Center for Turbulence Research: Annual Research Briefs*, pp. 197–208.
- DUPRET, F. & MARCHAL, J. M. 1986 Loss of evolution in the flow of viscoelastic liquids. *J. Non-Newtonian Fluid Mech.* **20**, 143–171.
- ECKELMANN, H. 1988 A review of knowledge on pressure fluctuations. In *Near-wall turbulence: 1988 Zoran Zaric Memorial Conference* (ed. S. J. Kline & N. H. Afgan), pp. 328–347. Hemisphere.
- GAMPERT, B. & YONG, C. 1989 The influence of polymer additives on the coherent structure of turbulent channel flow. In *IUTAM Symposium: Structure of Turbulence and Drag Reduction* (ed. A. Gyr), pp. 223–232. Springer.
- DE GENNES, P. G. 1990 *Introduction to Polymer Dynamics*. Cambridge University Press.
- GYR, A. & BEWERSDORFF, H.-W. 1995 *Drag Reduction of Turbulent Flows by Additives*. Kluwer.
- HARDER, K. J. & TIEDERMAN, W. G. 1991 Drag reduction and turbulent structure in two-dimensional channel flows. *Phil. Trans. R. Soc. Lond. A* **336**, 19–34.
- HERRCHEN, M. & ÖTTINGER, H. C. 1997 A detailed comparison of various FENE dumbbell models. *J. Non-Newtonian Fluid Mech.* **68**, 17–42.
- HINCH, E. J. 1977 Mechanical models of dilute polymer solutions in strong flows. *Phys. Fluids* **20**, S22–S30.
- HULSEN, M. A. 1990 A sufficient condition for a positive definite configuration tensor in differential models. *J. Non-Newtonian Fluid Mech.* **38**, 93–100.
- HULSEN, M. A., VAN HEEL, A. P. G. & VAN DEN BRULE, B. H. A. A. 1997 Simulation of viscoelastic flows using Brownian configuration fields. *J. Non-Newtonian Fluid Mech.* **70**, 79–101.
- HUNT, J. C. R. & DURBIN, P. A. 1999 Perturbed vortical layers and shear sheltering. *Fluid Dyn. Res.* **24**, 375–404.
- HUNT, J. C. R., MOIN, P., LEE, M., MOSER, R. D., SPALART, P., MANSOUR, N. N., KAIMAL, J. C. & GAYNOR, E. 1989 Cross correlation and length scales in turbulent flows near surfaces. In *Proc. Second European Turbulence Conference, Berlin, 1988* (ed. H.-H. Fernholz and H. E. Fiedler), pp. 128–134. Springer.
- HUNT, J. C. R. & MORRISON, A. 2000 Eddy structure in turbulent boundary layers. *Eur. J. Mech. B/Fluids* **19**, 673–694.
- JIMENEZ, J. & MOIN, P. 1991 The minimal flow unit in near-wall turbulence. *J. Fluid Mech.* **225**, 213–240.
- JOSEPH, D. D. 1990 *Fluid Dynamics of Viscoelastic Liquids*. Springer.
- JOSEPH, D. D. & SAUT, J. C. 1986 Change of type and loss of evolution in the flow of viscoelastic liquids. *J. Non-Newtonian Fluid Mech.* **20**, 117–141.
- KEUNINGS, R. K. 1989 Simulation of viscoelastic fluid flow. In *Fundamentals of Computer Modeling for Polymer Processing* (ed. C. L. Tucker III), pp. 403–469. Munich: Carl Hanser.
- KEUNINGS, R. K. 1997 On the Peterlin approximation for finitely extensible dumbbells. *J. Non-Newtonian Fluid Mech.* **68**, 85–100.

- KIM, J. 1989 On the structure of pressure fluctuations in simulated turbulent channel flow. *J. Fluid Mech.* **205**, 421–451.
- KIM, J., MOIN, P. & MOSER, R. 1987 Turbulence statistics in fully developed channel flow at low Reynolds numbers. *J. Fluid Mech.* **177**, 133–166.
- LUMLEY, J. L. 1969 Drag reduction by additives. *Annu. Rev. Fluid Mech.* **1**, 367–384.
- LUMLEY, J. L. 1973 Drag reduction in turbulent flow by polymer additives. *J. Polymer Sci.* **7**, 263–290.
- MCCOMB, W. D. & CHAN, K. T. J. 1985 Laser-Doppler anemometer measurements of turbulent structure in drag-reducing fibre suspensions. *J. Fluid Mech.* **152**, 455–478.
- MCCOMB, W. D. & RABIE, L. H. 1979 Development of local turbulent drag reduction due to nonuniform polymer concentration. *Phys. Fluids* **22**, 183–186.
- MCCOMB, W. D. & RABIE, L. H. 1982 Local drag reduction due to injection of polymer solutions into turbulent flow in a pipe. *AIChE J.* **28**, 547–565.
- MANSOUR, N. N., KIM, J. & MOIN, P. 1988 Reynolds-stress and dissipation-rate budgets in a turbulent channel flow. *J. Fluid Mech.* **194**, 15–44.
- MARCHAL, J. M. & CROCHET, M. J. 1987 A new mixed finite element for calculating viscoelastic flows. *J. Non-Newtonian Fluid Mech.* **26**, 77–114.
- MASSAH, H. & HANRATTY, T. J. 1997 Added stresses because of the presence of FENE-p bead-spring chains in a random velocity field. *J. Fluid Mech.* **337**, 67–101.
- MASSAH, H., KONTOMARIS, K., SCHOWALTER, W. R. & HANRATTY, T. J. 1993 The configurations of a FENE bead-spring chain in transient rheological flows and in turbulent flow. *Phys. Fluids* **5**, 881–889.
- MIN, T., YOO, J. Y. & CHOI, H. 2001 Effect of spatial discretization schemes on numerical solutions of viscoelastic fluid flow. *J. Non-Newtonian Fluid Mech.* **100**, 27–47.
- MIN, T., YOO, J. Y., CHOI, H. & JOSEPH, D. D. 2003 Drag reduction by polymer additives in a turbulent channel flow. *J. Fluid Mech.* **486**, 213–238.
- ORLANDI, P. 1995 A tentative approach to the direct simulation of drag reduction by polymers. *J. Non-Newtonian Fluid Mech.* **60**, 277–301.
- PINHO, F. T. & WHITELAW, J. H. 1990 Flow of non-newtonian fluids in a pipe. *J. Non-Newtonian Fluid Mech.* **34**, 129–144.
- PTASINSKI, P. K., NIEUWSTADT, F. T. M., VAN DEN BRULE, B. H. A. A. & HULSEN, M. A. 2001 Experiments in turbulent pipe flow with polymer additives at maximum drag reduction. *Flow, Turbulence Combust.* **66**, 159–182.
- SREENIVASAN, K. R. & WHITE, C. M. 2000 The onset of drag reduction by dilute polymer additives, and the maximum drag reduction asymptote. *J. Fluid Mech.* **409**, 149–164.
- SURESHKUMAR, R. & BERIS, A. N. 1995 Effect of artificial stress diffusivity on the stability of numerical calculations and the flow dynamics of time-dependent viscoelastic flows. *J. Non-Newtonian Fluid Mech.* **60**, 53–80.
- SURESHKUMAR, R., BERIS, A. N. & HANDLER, R. A. 1997 Direct numerical simulation of turbulent channel flow of a polymer solution. *Phys. Fluids* **9**, 743–755.
- TOMS, B. A. 1949 Some observations on the flow of linear polymer solutions through straight tubes at large Reynolds numbers. In *Proc. 1st Intl Congr. Rheol.*, pp. 135–141. North Holland.
- DEN TOONDER, J. 1995 Drag reduction by polymer additives in a turbulent pipe flow: Laboratory and numerical experiments. PhD thesis, Delft University of Technology.
- DEN TOONDER, J. M. J., HULSEN, M. A., KUIKEN, G. D. C. & NIEUWSTADT, F. T. M. 1997 Drag reduction by polymer additives in a turbulent pipe flow: numerical and laboratory experiments. *J. Fluid Mech.* **337**, 193–231.
- DEN TOONDER, J. M. J., NIEUWSTADT, F. T. M. & KUIKEN, G. D. C. 1995 The role of elongational viscosity in the mechanism of drag reduction by polymer additives. *Appl. Sci. Res.* **54**, 95–123.
- VAN DEN BRULE, B. H. A. A. 1993 Brownian dynamics simulation of finitely extensible bead-spring chains. *J. Non-Newtonian Fluid Mech.* **47**, 357–378.
- VIRK, P. S. 1975 Drag reduction fundamentals. *AIChE J.* **21**, 625–656.
- VIRK, P., MERRILL, E. W., MICKLEY, M. S., SMITH, K. & MOLLO-CHRISTENSEN, E. L. 1967 The toms' phenomenon: turbulent pipe flow of dilute polymer solutions. *J. Fluid Mech.* **30**, 305–328.
- VIRK, P., MICKLEY, H. & SMITH, K. 1970 The ultimate asymptote and mean flow structure in toms' phenomenon. *Trans. ASME: J. Appl. Mech.* **37**, 480–493.

- WARHOLIC, M. D., HEIST, D. K., KATCHER, M. & HANRATTY, T. J. 2001 A study with particle image velocimetry of the influence of drag-reducing polymers on the structure of turbulence. *Exps. Fluids* **31**, 474–483.
- WARHOLIC, M. D., MASSAH, H. & HANRATTY, T. J. 1999a Influence of drag-reducing polymers on a turbulence: effects of Reynolds number, concentration and mixing. *Exps. Fluids* **27**, 461–472.
- WARHOLIC, M. D., SCHMIDT, G. M. & HANRATTY, T. J. 1999b The influence of a drag-reducing surfactant on a turbulent velocity field. *J. Fluid Mech.* **388**, 1–20.
- WARNER, H. R. 1972 Kinetic theory and rheology of dilute suspensions of finitely extendible dumbbells. *Ind. Engng Chem. Fundam.* **11**, 379–387.
- WEDGEWOOD, L. E. & BIRD, R. B. 1988 From molecular models to the solution of flow problems. *Ind. Engng Chem. Res.* **27**, 1313–1320.
- WEI, T. & WILLMARTH, W. W. 1992 Modifying turbulent structure with drag-reducing polymer additives in turbulent channel flows. *J. Non-Newtonian Fluid Mech.* **245**, 619–641.
- WILCOX, D. C. 1993 *Turbulence Modeling for CFD*. Glendale: Griffin Printing.
- WILLMARTH, W., WEI, T. & LEE, C. 1987 Laser anemometer measurements of Reynolds stress in a turbulent channel flow with drag reducing polymer additives. *Phys. Fluids* **30**, 933–935.
- WILLMARTH, W. W. 1975 Pressure fluctuations beneath turbulent boundary layers. *Annu. Rev. Fluid Mech.* **7**, 13–38.
- WU, X., JACOBS, R. G., HUNT, J. C. R. & DURBIN, P. A. 1999 Simulation of boundary layer transition induced by periodically passing wakes. *J. Fluid Mech.* **398**, 109–153.